A EUROPEAN JOURNAL OF CHEMICAL BIOLOGY

CHEMBIOCHEM

SYNTHETIC BIOLOGY & BIO-NANOTECHNOLOGY

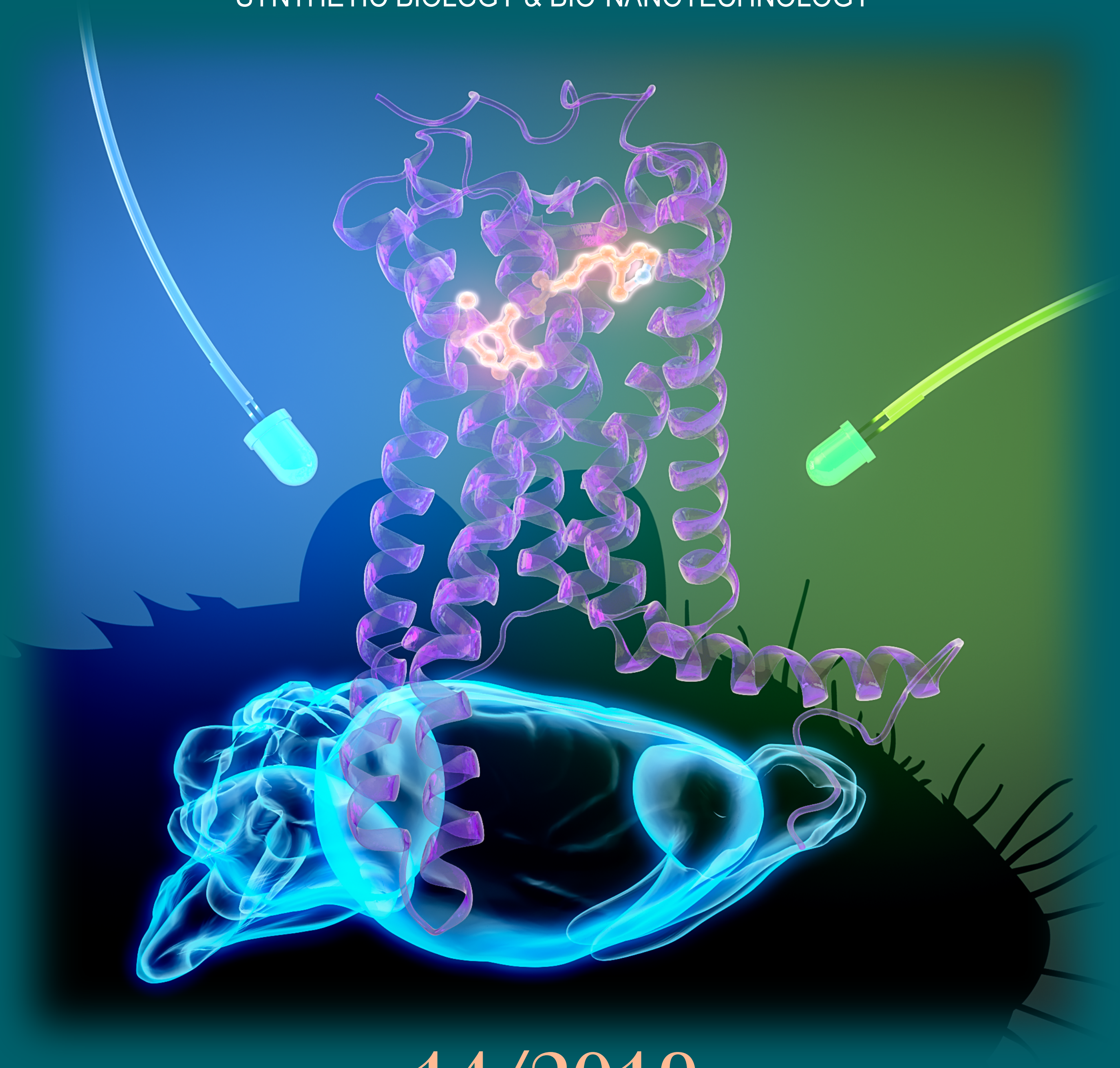

14/2019

Cover Feature:
S. Herlitze, K. Gerwert et al.
Design of an Ultrafast G Protein Switch Based
on a Mouse Melanopsin Variant

A Journal of
ChemPubSoc Europe

WILEY-VCH

www.chembiochem.org

ChemPubSoc Europe
DOI: 10.1002/cbic.201900110
CHEMBIOCHEM
Communications

Design of an Ultrafast G Protein Switch Based on a Mouse Melanopsin Variant

Stefan Alexander Tennigkeit+,[a] Raziye Karapinar+,[b] Till Rudack+,[a] Max-Aylmer Dreier,[a] Philipp Althoff,[a] Dennis Eickelbeck,[b] Tatjana Surdin,[b] Michelle Grömmke,[b] Melanie D. Mark,[b] Katharina Spoida,[b] Mathias Lübben,[a] Udo Höweler,[c] Stefan Herlitze,*[b] and Klaus Gerwert*[a]

The primary goal of optogenetics is the light-controlled noninvasive and specific manipulation of various cellular processes. Herein, we present a hybrid strategy for targeted protein engineering combining computational techniques with electrophysiological and UV/visible spectroscopic experiments. We validated our concept for channelrhodopsin-2 and applied it to modify the less-well-studied vertebrate opsin melanopsin. Melanopsin is a promising optogenetic tool that functions as a selective molecular light switch for G protein-coupled receptor pathways. Thus, we constructed a model of the melanopsin G_q protein complex and predicted an absorption maximum shift of the Y211F variant. This variant displays a narrow blue-shifted action spectrum and twofold faster deactivation kinetics compared to wild-type melanopsin on G protein-coupled inward rectifying K^+ (GIRK) channels in HEK293 cells. Furthermore, we verified the in vivo activity and optogenetic potential for the variant in mice. Thus, we propose that our developed concept will be generally applicable to designing optogenetic tools.

Light is vital for most living organisms. The ability to sense and respond to light is mediated by different light-sensitive proteins.[1] Optogenetics is an innovative technique combining the use of light-sensitive proteins and genetically targeted cells in organisms to precisely perform light-controlled manipulation of cell function and signaling.[2] A prerequisite for the targeted engineering of light-sensitive proteins to be used as precise noninvasive optogenetic tools is a detailed atomistic understanding of photoactivatable biological processes.

By now microbial rhodopsins are the best-studied optogenetic tools.[3,4] Bacteriorhodopsin (bR),[5] the first discovered representative of this class, inspired the development of novel biophysical tools for structural and functional investigation. Microbial rhodopsins span the membrane by seven transmembrane helices and comprise the chromophore retinal, which is covalently bound to a lysine through a protonated Schiff base. Fundamental research has enabled us to understand the structure and function of bR[6,7] and paved the way for studies of many additional microbial rhodopsins. Among these is the currently most widely used optogenetic tool channelrhodopsin-2 (ChR2), a light-gated ion channel from *Chlamydomonas reinhardtii* belonging to the type I opsins.[3,4,8] Since the usefulness of ChR2 in optogenetics has been established, many improved variants have been designed.[9,10]

Other key players in optogenetics are type II (animal) opsins belonging to the family of G protein-coupled receptors (GPCRs). Once activated by light, the GPCR in complex with specific G proteins activates second messengers and signaling pathways to control a variety of vital physiological processes, for example, vision.[11] We have studied the photoreceptor GPCR melanopsin from vertebrates, which occurs in intrinsically photosensitive retinal ganglion cells (ipRGCs) being mainly involved in nonvision processes.[12,13]

In optogenetic experiments, melanopsin operates as a selective molecular switch with limited phototoxicity. It is a tristable opsin that enables a precise control of the activation and deactivation of GPCR pathways and/or neuronal firing,[14,15] which is switched on by blue light and off by yellow light.[16] G protein transduction is divided into two classes: the cAMP signal pathway and phosphatidylinositol bisphosphate (PIP_2) pathway. G_i inhibits the cAMP signal pathway and G_q activates the PIP_2 pathway. Whereas vertebrate ciliary photoreceptors usually activate the G_t pathway,[17] melanopsin is one of the few known vertebrate opsins to be capable of activating $G_{q/11}$ signaling in neurons. Other light-activated GPCRs are vertebrate cone opsins (i.e., short-wave (vSWO) and long-wave (vLWO) opsins), which solely activate the $G_{i/o}$ pathway. vSWO- and vLWO-mediated $G_{i/o}$ pathway activation in neurons are maximally induced by UV light and red light, respectively,[18] whereas melanopsin-mediated $G_{q/11}$ pathway activation in neurons is maximally induced by blue light.[19]

A long-term goal is to specifically light activate and deactivate distinct G protein-coupled pathways by using melanopsin in parallel with a distinct vertebrate opsin expressed in the

---

[a] *S. A. Tennigkeit,+ T. Rudack,+ M.-A. Dreier, P. Althoff, M. Lübben,*
Prof. Dr. K. Gerwert
Department of Biophysics, Ruhr University Bochum
Universitätsstrasse 150, 44780 Bochum (Germany)
E-mail: klaus.gerwert@bph.rub.de

[b] *R. Karapinar,+ D. Eickelbeck, T. Surdin, M. Grömmke, M. D. Mark, K. Spoida,*
Prof. Dr. S. Herlitze
Department of General Zoology and Neurobiology, Ruhr University Bochum
Universitätsstrasse 150, 44780 Bochum (Germany)
E-mail: sxh106@gmail.com

[c] *U. Höweler*
Westfälische Wilhelms-Universität Münster, Organisch-Chemisches Institut
Corrensstrasse 40, 48149 Münster (Germany)

[+] *These authors contributed equally to this work.*

Supporting information and the ORCID identification numbers for the authors of this article can be found under https://doi.org/10.1002/cbic.201900110.

same cell. However, crosstalk between the absorption bands of melanopsin and cone opsins might exist. To optimize the optogenetic performance of melanopsin in combination with cone opsins for in vivo applications, the excitation overlap of these proteins has to be eliminated by engineering a +melanopsin variant with blue-shifted activation spectrum (Figure S1 in the Supporting Information). However, changing the wavelength dependency ("color tuning") of melanopsin by trial-and-error experimental methods usually involves tedious human work. Therefore, a knowledge-based approach considering the structure–wavelength relationship is desired to lead to a systematic protein-engineering strategy that reduces human work for color tuning.

Biomolecular simulations are a useful tool to gain information for such a systematic strategy. In fact, the introduction of hybrid quantum mechanics and molecular mechanics (QM/MM) simulations[20] enabled the first calculated UV/Vis spectrum and color-tuning studies of the retinal protein bR,[21] ChR2,[22] and of melanopsin.[23] Theoretical UV/Vis spectroscopy allows the calculation of excitation energies, provided that structural models of the involved proteins are accessible. In order to obtain a reliable prediction of the structure–wavelength relationship for targeted color tuning, a careful validation of the UV/Vis calculation approach is needed. Especially as there is a huge variety of conceptually different approaches (semi-empirical or density functional theory (DFT)) to set up and calculate excitation energies; the determination of the appropriate approach is of particular importance.[24] Therefore, in this work, we first used the well-studied ChR2[3,4,8,25,26] to validate and establish our UV/Vis spectra calculation workflow, which then enabled us to predict a melanopsin variant with shifted absorption maximum (λ_{max}).

Initially, we identified putative mutations for a red-shifted λ_{max} of ChR2, because the radiation of red light is less harmful to tissue and has a deeper penetration depth. Figure S2A shows the sequence alignment of several microbial rhodopsins, for example, Chrimson,[27] which are known to have a red-shifted λ_{max} compared to ChR2.[5,28–30] Combining this sequence information with the structural information from the ChR2 X-ray structure (PDB ID: 6EID;[31] Figure S2 B), we considered only those residues in close proximity to the retinal. Our analysis yielded four novel ChR2 variants (K93F, G181S, S256A and K93F/S256A; Figure 1 A) not yet discussed in the literature. These variants affect the local polarity within the retinal binding pocket. We made UV/Vis spectroscopic measurements to demonstrate that all these mutants have a red-shifted λ_{max} (Figure 1 B and Table 1).

Concurrent λ_{max} shifts of the ChR2 variants described above were calculated by employing the theoretical UV/Vis spectroscopy workflow detailed in Supporting Note 1 and in Figure S4. The recently resolved X-ray structure of ChR2[31] was used as the initial structural model. Excitation energies were calculated by using three different conceptual approaches; the semi-empirical CI method with modified neglect of diatomic overlap (MNDOC) parameters[32] and two different DFT approaches, namely TD/631-G*, and RCIS=(FC)/6-31G*.[24] The measured and calculated λ_{max} shifts are compared in Table 1, which reveals that all methods predict a red shift of the ChR2 mutants; this is in full accordance with the experiment (Figure 1 B). Therefore, from here on, we used only the fastest and computationally cheapest semiempirical CI method with MNDOC parameters available to us; this allows for the necessary QM/MM coupling.

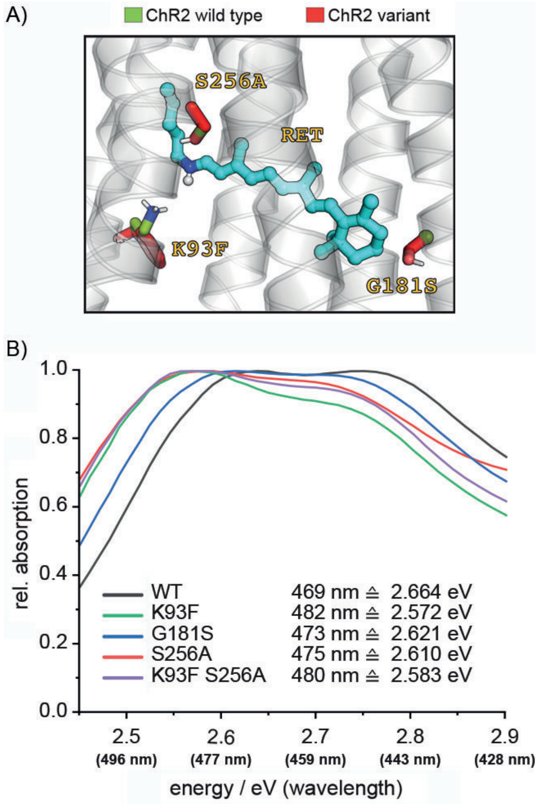

Figure 1. UV/Vis spectroscopy of ChR2 variants. A) The ChR2 all-*trans* retinal (cyan) binding pocket, based on PDB ID: 6EID,[31] with site-specific variants highlighted. B) The experimentally determined absorption spectra of all ChR2 variants were red-shifted with respect to that of WT. See also Figure S3 and Table 1.

Table 1. Measured and calculated UV/Vis absorption shifts of ChR2 wild-type and site-specific variants. The average shifts of both monomers are given; absolute values are presented in Table S1.

	UV/Vis absorption shifts [eV]			
	Measured	MNDOC	TD/6-31G*	RCIS=(FC)/6-31G*
G181S	−0.022	−0.019	−0.030	−0.030
S256A	−0.034	−0.039	−0.038	−0.037
K93F	−0.072	−0.043	−0.029	−0.030
K93F/S256A	−0.061	−0.049	−0.043	−0.042

Our theoretical UV/Vis spectroscopy approach enables us to predict the shift direction of the absorption maximum of variants. Through this prediction, we reduce the number of experimentally measured variants to a small pool of promising candidates. Such targeted selection of candidates is more economic than strictly random trial-and-error experiments.

Correct prediction of the structure–wavelength relation strongly depends on the quality of the structural model used to initiate the excitation energy calculations. In contrast to ChR2, the 3D structure of melanopsin has not yet been experimentally determined. However, recent breakthroughs in structural biology allowed structural models of opsins to be obtained by X-ray crystallography,[33–35] cryo-electron microscopy,[36,37] and homology modeling.[23] Using these structural data, we constructed an atomistic model of membrane-inserted solvated melanopsin G_q protein complex. As outlined in Supporting Note 2 and Figure S5, we optimized the modeling concept, which was initially developed to build soluble proteins like the proteasome,[38] to create structural models of transmembrane proteins. The key benefit of this concept is to streamline and facilitate the use of established but often complicated modeling suites like Rosetta and Modeller for ab initio structure prediction and homology modeling.

For homology modeling of free melanopsin (i.e., not in complex with G proteins), we chose the same template as Sekharan et al.,[23] a squid rhodopsin.[34] However, the model of Sekharan et al. erroneously introduced an extra isoleucine into the mouse melanopsin sequence at position 129. Our corrected sequence alignment is shown in Figure 2 A. Figure 2 B reveals that the similarity between melanopsin and squid rhodopsin is sufficient to build a reliable model exhibiting a similarity of 68 % within the modeled sequence region. Table S2 reflects that within the retinal binding pocket region (all amino acids within 10 Å distance of the retinal) the sequence similarity reaches 79 %. A correct assignment is further ensured by the marked anchor residues (Figure 2 A) considered to be residues in the helical region that are identical in the sequence alignment. The helical regions, highlighted in green, were identified by using a variety of different computational tools, as outlined in Figure S6.

Next, the melanopsin G_q protein complex was modeled as detailed in the Supporting Note 2: The X-ray structure of β_2AR in complex with the G_s protein[33] served as the basis for the binary complex model (Figures S7 and S8). The resulting struc-

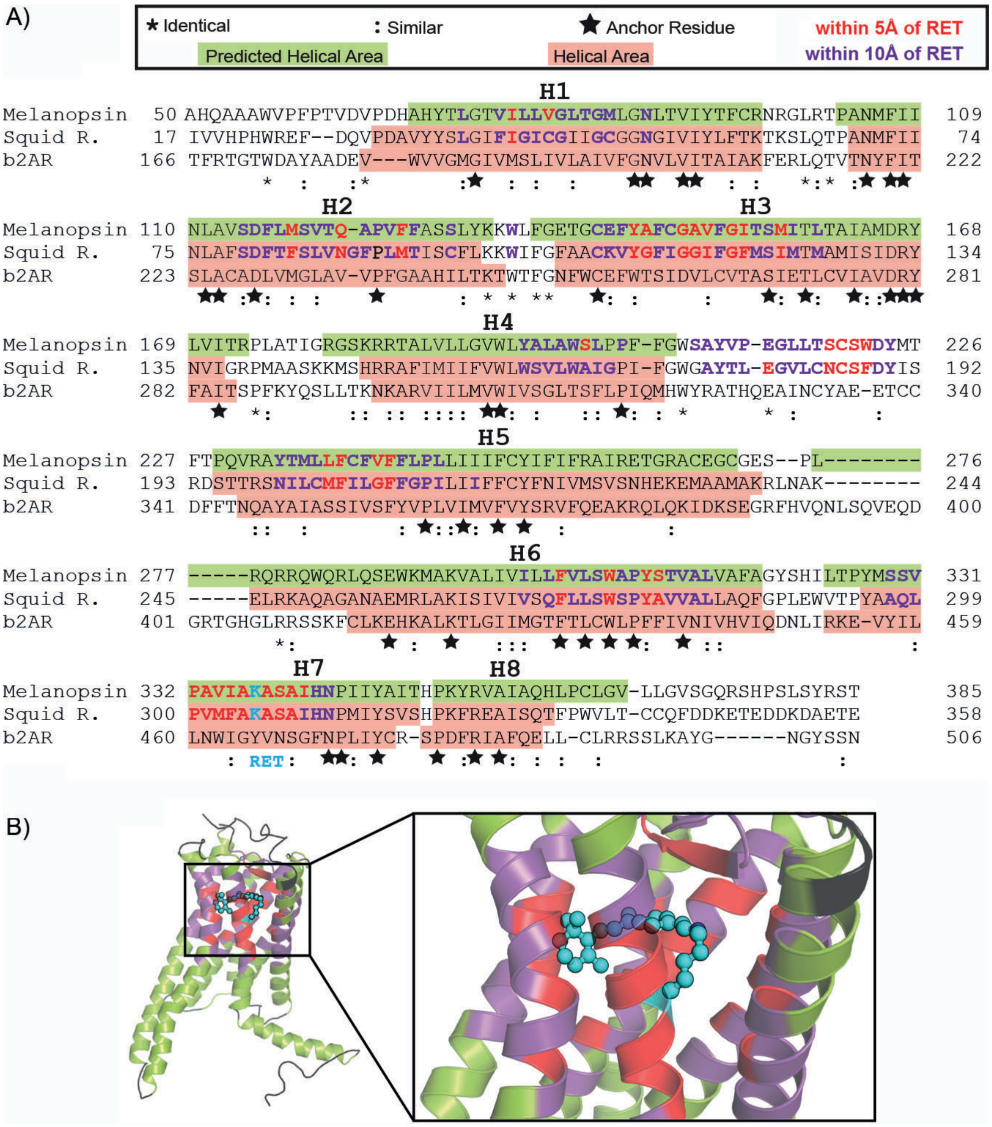

Figure 2. Melanopsin model construction. A) Sequence alignment of melanopsin with squid rhodopsin[34] and β_2AR.[33] The residues within 5 Å of the retinal are written in red and those 5–10 Å from retinal are in purple. The predicted helices are highlighted in green (Figure S6), and the helical residues of the X-ray structures are in pink. B) Final melanopsin homology model.

ture was then used to initiate a 100 ns molecular mechanics (MM) equilibration. In five subsequent independent MM production runs (100 ns each), the protein-backbone-forming Cα atom positions converged as shown by their root mean square deviations (RMSD; Figure S9). Thus, we consider the structural model obtained to be stable and reliable.

To calculate the theoretical UV/Vis spectra, we adopted the approach we used for ChR2, starting by identifying hot spots for amino acid exchange in melanopsin. Here, we focused on the residues in the area between 5 and 10 Å from retinal (Figure S10). These residues are close enough to the retinal to have a significant electrostatic influence; however, they are also likely far enough away to keep the overall structure and function of melanopsin intact. We identified Y211F (Figure 4A) as a promising variant for which we calculated a blue-shifted λ_{max} of +0.016 eV.

We characterized the biophysical, optogenetic properties of Y211F melanopsin by using patch-clamp recordings in HEK293 cells with stable expressing G protein-coupled inward rectifying K^+ (GIRK) 1,2 channels. In these cells, light-activated melanopsins result in a $G_{i/o}$-pathway-mediated GIRK current. (Note, in neurons melanopsin activates mainly the $G_{q/11}$ pathway, whereas in HEK293 cells it activates the $G_{i/o}$ and the $G_{q/11}$ pathways.[16]) As predicted, the Y211F variant reveals a blue-shifted λ_{max} in the activation action spectrum at 450 nm (2.755 eV) compared to 470 nm (2.638 eV) for WT melanopsin (Figure 3 and the Supporting Note 3). The action spectrum (Figure 3B) reveals a narrower shape for Y211F than for the WT. Both completely deactivate GIRK currents at 560 nm (2.214 eV, Figure S11). The resulting 20 nm (0.117 eV) shift during light-induced activation is somewhat larger than predicted.

Furthermore, we characterized the activation and deactivation of melanopsin-induced GIRK currents (Figure 3C and D). The activation and deactivation kinetics determine how fast a cellular pathway can be controlled by light. The melanopsin-dependent, light-induced GIRK current activation and deactivation of variant Y211F ($\tau_{on} \approx 1.0$ s; $\tau_{off} \approx 5.0$ s) are faster than in WT melanopsin ($\tau_{on} \approx 1.4$ s; $\tau_{off} \approx 8.9$ s). The Y211F variant also reveals a transient activation of the G protein pathways (Figure 3C), as becomes obvious in the 45% decline in response amplitude for Y211F in comparison to for WT (15%) when melanopsins are deactivated after 30 s (Figures 3C and S12A, B).

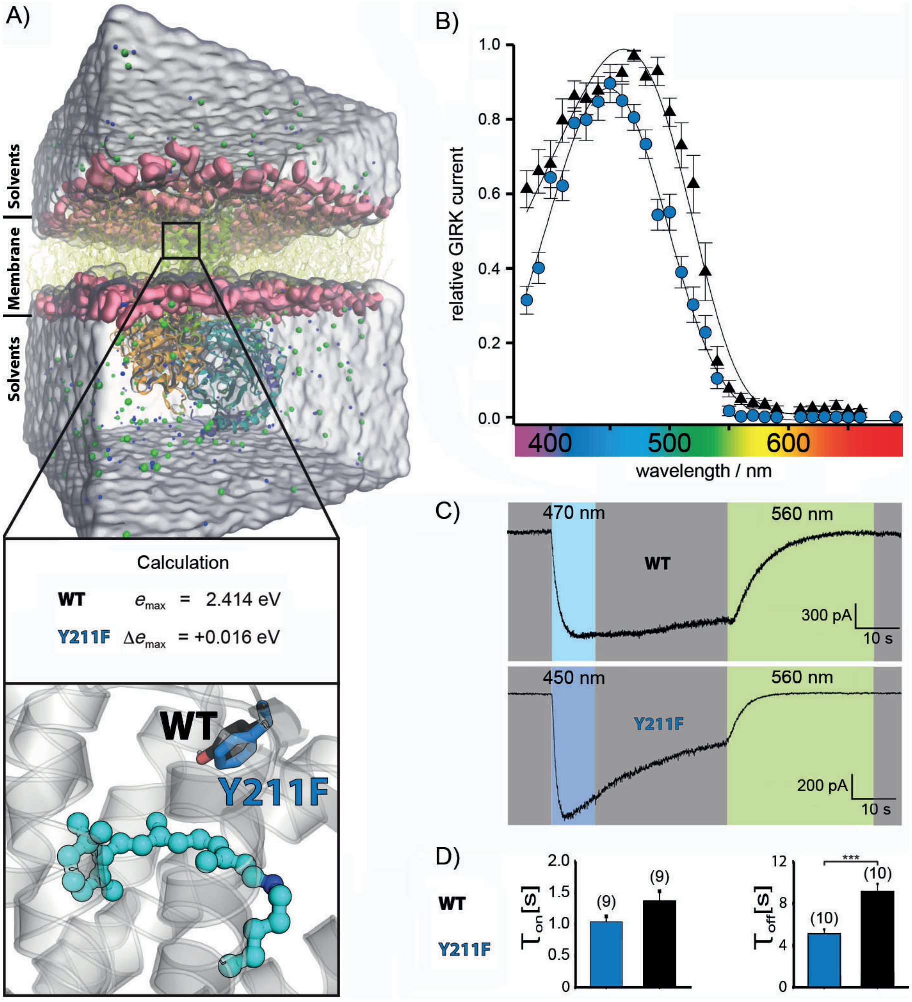

Figure 3. In silico and in vitro characterization of the Y211F variant. A) Simulation system of the melanopsin G_q protein complex with the retinal binding pocket enlarged and the calculated λ_{max} shift of the Y211F variant. B) Wavelength dependency of a normalized light-induced GIRK currents evoked by WT (▲) and Y211F (●) activation ($n=7$ cells). C) Comparison of GIRK current traces induced by WT and Y211F. D) Comparison of the activation (τ_{on}, $n=9$ cells) and deactivation (τ_{off}, $n=10$ cells) time constants of Y211F and WT melanopsin.

However, light-activated, Y211F-mediated responses do not decline in amplitude when deactivation occurs immediately after activation. This allows for repetitive, fast, long-term stimulation of the G protein pathway (Figure S13A), which is currently not possible with other melanopsin variants.[16] The fast temporal control of the G protein pathway is possible because of the fast activation and deactivation kinetics of Y211F (Figure 3D). Thus, Y211F is an ideal tool to control intracellular G protein signals repetitively with very low phototoxicity. (For a detailed characterization of our variant see Supporting Note 4 and Figures S11–S15.)

We next analyzed the potential of combining our tuned melanopsin variant with $G_{i/o}$-pathway-activating vertebrate cone opsins for simultaneous optogenetic control of two independent G protein pathways in vivo. As it has a narrow action spectrum, Y211F can be combined with vertebrate $G_{i/o}$ coupled short-wave opsin (vSWO) and long-wave opsin (vLWO). As shown in Figure 4A vSWO can be activated at 380 nm (100% activity) with negligible crosstalk with Y211F melanopsin, which is only 31% active, compared to 61% of WT. Equally, activation of Y211F at 480 nm (75%) leads to negligible activation of vSWO (20%). On the other hand, Y211F can be activated at 420 nm (80%) with negligible crosstalk with vLWO activation (<30%; Figure 4B). Y211F can be deactivated at 560 nm without activation of Y211F (0%) or vSWO (0%; Figure 4A), but with strong activation of vLWO (>75%; Figure 4B). Thus, combining Y211F melanopsin either with vSWO or vLWO is a promising optogenetic strategy for the specific activation and deactivation of different G protein pathways in vivo.

As a first step towards in vivo application, we demonstrated that Y211F optogenetically controls neuronal firing. We expressed Y211F specifically in Purkinje cells (PC; Figure 5A), an important neuron type in the cerebellum for integrating motor commands and adjusting motor behavior. As shown in Figure 5, 10 s pulses of blue light increase the firing frequency of PC. These proof-of-principle experiments demonstrate a promising optogenetic potential for in vivo application of the Y211F melanopsin variant.

In conclusion, we have presented a hybrid concept for targeted protein engineering. We have established a UV/Vis spectra calculation workflow and constructed a homology model of the melanopsin G_q protein complex. With this approach, we identified the Y211F melanopsin variant. Electrophysiological experiments revealed that the variant exhibits enhanced temporal precision for controlling G protein signals, with faster activation and twofold faster deactivation kinetics than WT mela-

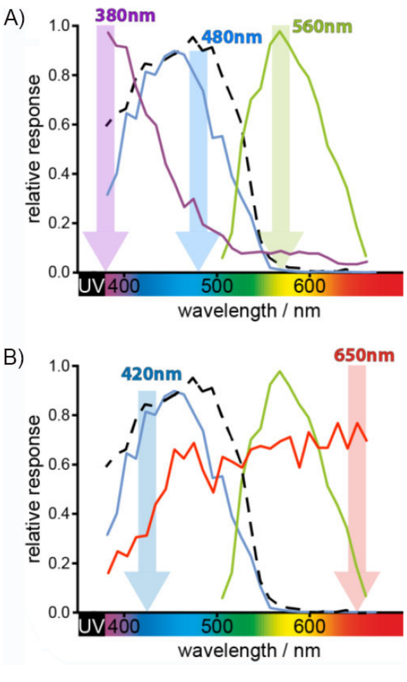

Figure 4. Potential optogenetic application of Y211F melanopsin. A) Distinct activation of vSWO (——) at 380 nm as well as Y211F (——) at 480 nm and deactivation of Y211F (——) at 560 nm with negligible excitation energy overlap. B) The transient character of the Y211F melanopsin variant now allows its combination with vLWO (——), as it does not need to be switched off anymore; Y211F melanopsin can be activated at 420 nm and vLWO at 650 nm. vLWO and vSWO data are from our previous publication.[18] All graphs represent normalized light induced GIRK currents; WT (-----) is shown for comparison.

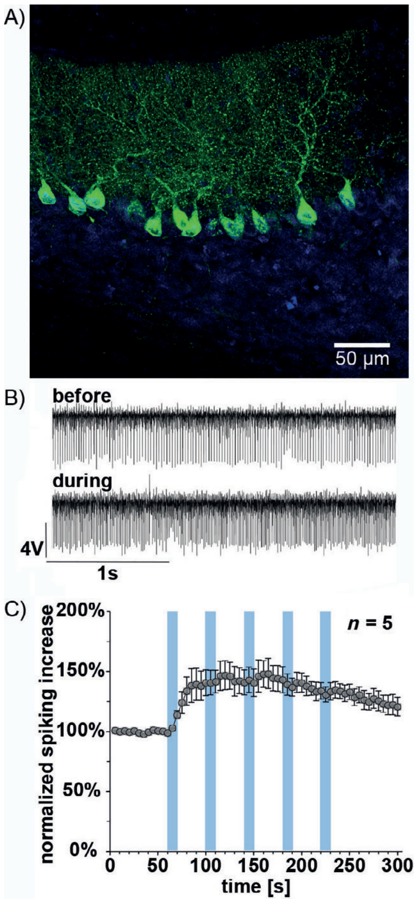

Figure 5. In vivo characterization of Y211F melanopsin. A) Adeno-associated virus (AAV)-mediated expression of yellow fluorescent protein (YFP)-tagged Y211F melanopsin (green) in cerebellar Purkinje cells. Blue shows where the PCs are stained with Nissl. B) Example in vivo traces of spiking cerebellar PC before and during light application. C) activation of Y211F expressed in cerebellar PCs by 10 s pulses of light (■) increases the firing frequency of PCs. Average: change in normalized firing frequency of five cells of one mouse.

nopsin. In addition, the narrow action spectrum makes our variant a promising candidate for combined activation with the cone opsins vSWO and vLWO for specific activation and deactivation of different G protein pathways in the brain and other tissues.

Acknowledgements

We thank Gabi Smuda for technical support, the Deutsche Forschungsgemeinschaft He2471/23-1, He2471/21-1, He2471/19-1 Priority Program (SPP1926), SFB874 (B10), SFB1280 (A07), Deutsche Studiensstiftung, and the Friedrich-Ebert-Stiftung for financial support.

Conflict of Interest

The authors declare no conflict of interest.

Keywords: computational chemistry · electrophysiology · integrative modeling · mutagenesis · structural biology

[1] O. P. Ernst, D. T. Lodowski, M. Elstner, P. Hegemann, L. S. Brown, H. Kandori, *Chem. Rev.* **2014**, *114*, 126–163.
[2] K. Deisseroth, *Nat. Methods* **2011**, *8*, 26–29.
[3] E. S. Boyden, F. Zhang, E. Bamberg, G. Nagel, K. Deisseroth, *Nat. Neurosci.* **2005**, *8*, 1263–1268.
[4] G. Nagel, T. Szellas, W. Huhn, S. Kateriya, N. Adeishvili, P. Berthold, D. Ollig, P. Hegemann, E. Bamberg, *Proc. Natl. Acad. Sci. USA* **2003**, *100*, 13940–13945.
[5] D. Oesterhelt, W. Stoeckenius, *Nat. New Biol.* **1971**, *233*, 149–152.
[6] K. Gerwert, B. Hess, J. Soppa, D. Oesterhelt, *Proc. Natl. Acad. Sci. USA* **1989**, *86*, 4943–4947.
[7] F. Garczarek, K. Gerwert, *Nature* **2006**, *439*, 109–112.
[8] X. Li, D. V. Gutierrez, M. G. Hanson, J. Han, M. D. Mark, H. Chiel, P. Hegemann, L. T. Landmesser, S. Herlitze, *Proc. Natl. Acad. Sci. USA* **2005**, *102*, 17816–17821.
[9] J. Y. Lin, M. Z. Lin, P. Steinbach, R. Y. Tsien, *Biophys. J.* **2009**, *96*, 1803–1814.
[10] J. Y. Lin, *Exp. Physiol.* **2011**, *96*, 19–25.
[11] S. Hughes, M. W. Hankins, R. G. Foster, S. N. Peirson in *Progress in Brain Research* (Eds.: A. Kalsbeek, M. Merrow, T. Roenneberg, R. G. Foster), Elsevier, **2012**, pp. 19–40.
[12] S. Herlitze, L. T. Landmesser, *Curr. Opin. Neurobiol.* **2007**, *17*, 87–94.
[13] M. W. Hankins, S. N. Peirson, R. G. Foster, *Trends Neurosci.* **2008**, *31*, 27–36.
[14] A. J. Emanuel, M. T. H. Do, *Neuron* **2015**, *85*, 1043–1055.
[15] K. Spoida, O. A. Masseck, E. S. Deneris, S. Herlitze, *Proc. Natl. Acad. Sci. USA* **2014**, *111*, 6479–6784.
[16] K. Spoida, D. Eickelbeck, R. Karapinar, T. Eckhardt, M. D. Mark, D. Jancke, B. V. Ehinger, P. König, D. Dalkara, S. Herlitze, O. A. Masseck, *Curr. Biol.* **2016**, *26*, 1206–1212.
[17] Y. Shichida, H. Imai, *Cell. Mol. Life Sci.* **1998**, *54*, 1299–1315.
[18] O. A. Masseck, K. Spoida, D. Dalkara, T. Maejima, J. M. Rubelowski, L. Wallhorn, E. S. Deneris, S. Herlitze, *Neuron* **2014**, *81*, 1263–1273.
[19] S. Panda, S. K. Nayak, B. Campo, J. R. Walker, J. B. Hogenesch, T. Jegla, *Science* **2005**, *307*, 600–604.
[20] A. Warshel, M. Levitt, *J. Mol. Biol.* **1976**, *103*, 227–249.
[21] M. Hoffmann, M. Wanko, P. Strodel, P. H. König, T. Frauenheim, K. Schulten, W. Thiel, E. Tajkhorshid, M. Elstner, *J. Am. Chem. Soc.* **2006**, *128*, 10808–10818.
[22] A. Ardevol, G. Hummer, *Proc. Natl. Acad. Sci. USA* **2018**, *115*, 3557–3562.
[23] S. Sekharan, J. N. Wei, V. S. Batista, *J. Am. Chem. Soc.* **2012**, *134*, 19536–19539.
[24] H. M. Senn, W. Thiel, *Angew. Chem. Int. Ed.* **2009**, *48*, 1198–1229; *Angew. Chem.* **2009**, *121*, 1220–1254.
[25] K. Eisenhauer, J. Kuhne, E. Ritter, A. Berndt, S. Wolf, E. Freier, F. Bartl, P. Hegemann, K. Gerwert, *J. Biol. Chem.* **2012**, *287*, 6904–6911.
[26] J. Kuhne, K. Eisenhauer, E. Ritter, P. Hegemann, K. Gerwert, F. Bartl, *Angew. Chem. Int. Ed.* **2015**, *54*, 4953–4957; *Angew. Chem.* **2015**, *127*, 5037–5041.
[27] K. Oda, J. Vierock, S. Oishi, S. Rodriguez-Rozada, R. Taniguchi, K. Yamashita, J. S. Wiegert, T. Nishizawa, P. Hegemann, O. Nureki, *Nat. Commun.* **2018**, *9*, 3949.
[28] N. C. Klapoetke, Y. Murata, S. S. Kim, S. R. Pulver, A. Birdsey-Benson, Y. K. Cho, T. K. Morimoto, A. S. Chuong, E. J. Carpenter, Z. Tian, et al., *Nat. Methods* **2014**, *11*, 338–346.
[29] B. S. Krause, C. Grimm, J. C. D. Kaufmann, F. Schneider, T. P. Sakmar, F. J. Bartl, P. Hegemann, *Biophys. J.* **2017**, *112*, 1166–1175.
[30] J. Y. Lin, P. M. Knutsen, A. Muller, D. Kleinfeld, R. Y. Tsien, *Nat. Neurosci.* **2013**, *16*, 1499–1508.
[31] O. Volkov, K. Kovalev, V. Polovinkin, V. Borshchevskiy, C. Bamann, R. Astashkin, E. Marin, A. Popov, T. Balandin, D. Willbold, G. Büldt, E. Bamberg, V. Gordeliy, *Science* **2017**, *358*, eaan8862.
[32] W. Thiel, *J. Am. Chem. Soc.* **1981**, *103*, 1413–1420.
[33] S. G. F. Rasmussen, B. T. DeVree, Y. Zou, A. C. Kruse, K. Y. Chung, T. S. Kobilka, F. S. Thian, P. S. Chae, E. Pardon, D. Calinski, et al., *Nature* **2011**, *477*, 549–555.
[34] M. Murakami, T. Kouyama, *Nature* **2008**, *453*, 363–367.
[35] M. E. Sommer, M. Elgeti, P. W. Hildebrand, M. Szczepek, K. P. Hofmann, P. Scheerer in *Methods in Enzymology, Vol. 556:* ***Membrane Proteins****: Production and Functional Characterization* (Ed.: A. K. Shukla), Academic Press, San Diego, **2015**, pp. 563–608.
[36] Y.-L. Liang, M. Khoshouei, G. Deganutti, A. Glukhova, C. Koole, T. S. Peat, M. Radjainia, J. M. Plitzko, W. Baumeister, L. J. Miller, et al., *Nature* **2018**, *561*, 492–497.
[37] Y.-L. Liang, M. Khoshouei, M. Radjainia, Y. Zhang, A. Glukhova, J. Tarrasch, D. M. Thal, S. G. B. Furness, G. Christopoulos, T. Coudrat, R. Danev, W. Baumeister, L. J. Miller, A. Christopoulos, B. K. Kobilka, D. Wootten, G. Skiniotis, P. M. Sexton, *Nature* **2017**, *546*, 118–123.
[38] M. Wehmer, T. Rudack, F. Beck, A. Aufderheide, G. Pfeifer, J. M. Plitzko, F. Förster, K. Schulten, W. Baumeister, E. Sakata, *Proc. Natl. Acad. Sci. USA* **2017**, *114*, 1305–1310.

Manuscript received: February 19, 2019
Accepted manuscript online: March 28, 2019
Version of record online: ■■ ■■, 0000

A hybrid strategy for targeted protein engineering combines computational chemistry with electrophysiological and UV/Vis spectroscopic experiments. Using this strategy, we designed and characterized a site-specific variant of the molecular light switch melanopsin that, in combination with other vertebrate opsins, makes a promising optogenetic tool for selective control of two different G protein pathways.

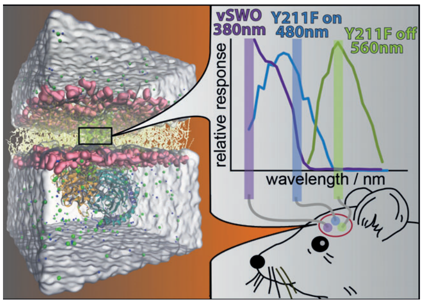

S. A. Tennigkeit, R. Karapinar, T. Rudack, M.-A. Dreier, P. Althoff, D. Eickelbeck, T. Surdin, M. Grömmke, M. D. Mark, K. Spoida, M. Lübben, U. Höweler, S. Herlitze, K. Gerwert**

■■ – ■■

Design of an Ultrafast G Protein Switch Based on a Mouse Melanopsin Variant

CHEMBIOCHEM

Supporting Information

Design of an Ultrafast G Protein Switch Based on a Mouse Melanopsin Variant

Stefan Alexander Tennigkeit+,[a] Raziye Karapinar+,[b] Till Rudack+,[a] Max-Aylmer Dreier,[a]
Philipp Althoff,[a] Dennis Eickelbeck,[b] Tatjana Surdin,[b] Michelle Grömmke,[b]
Melanie D. Mark,[b] Katharina Spoida,[b] Mathias Lübben,[a] Udo Höweler,[c] Stefan Herlitze,*[b]
and Klaus Gerwert*[a]

cbic_201900110_sm_miscellaneous_information.pdf

Supporting Information

Material and Methods

Experimental Methods

Yeast culture

Pichia pastoris strain SMD1163 cells (kind gift from C. Bamann) containing the pPIC9KChR2His10 construct were precultured in BMGY medium[1]. Expression of ChR2 was induced in BMMY medium containing 2.5 µM all-*trans* retinal and 0.00004% biotin at an initial OD_{600} of 1 and at 30 °C and 120 rpm. Cells were harvested at an OD_{600} of 20 by centrifugation.

Membrane preparation and protein purification

Cells were disrupted using a BeadBeater (Biospec Products) and membranes were isolated by ultracentrifugation. Homogenized membranes were solubilized with 1% decyl maltoside overnight. ChR2 purification was done by Ni-NTA affinity chromatography and subsequent gelfiltration using a HiLoad 16/600 Superdex 200 pg column (GE).

UV/VIS measurements

Purified, solubilized protein samples were measured at ambient temperatures using a MMS UV/VIS I diode array (Zeiss) with 256 diodes covering 190-720 nm and a 12-bit A/D converter. A halogen and a deuterium lamp were used as a light source. Samples were measured against buffer solution (20 mM HEPES pH 7.5, 100 mM NaCl, 0.15% DM) without protein.

Generation of plasmid constructs

The long isoform of mouse melanopsin (mOpn4L or moMo, GenBank accession number: NM_013887.2) was used as the backbone construct for the generation of the Y211F variant. To construct AAV-expression vectors, the pAAV-CMV-EGFP vector (Stratagene) was used as the backbone plasmid for the virus. The sequence of mouse melanopsin was PCR amplified with 16 bp overhangs and inserted into the backbone via AQUA Cloning, replacing the DNA sequences between the inverted terminal repeats (ITR sites). To introduce the point mutation by the primer extension method, primer including the point mutation Y211F 5´- CTT TGG TTG GAG TGC CTT CGT GCC

CGA GGG GCT-3´and 5´-AGC AGC CCC TCG GGC ACG AAG GCA CTC CAA CCA-3´ were used.

Cell culture

Human embryonic kidney (HEK) tsA 201 cells stably expressing GIRK channels (kindly provided by Dr. A. Tinker UCL London, GB), were maintained at 37 °C in Dulbecco's modified Eagle's medium (DMEM), 4.5 g l^{-1}D-glucose, supplemented with 10% fetal bovine serum (Gibco) and penicillin/streptomycin in a humidified incubator under 5% CO_2. Growth medium of stable cell lines was supplemented with G418 (5 mg/ml). Cells were transfected with FuGENE® HD (Promega) according to the manufacturer's protocol and incubated for 24 h before whole cell recordings. Retinal (all-*trans* retinal with no difference detectable, see[2]) was added to a final medium concentration of 1 µM.

In vitro whole cell recordings

HEK cell recordings: For GIRK channel recordings light-sensitive GPCRs were expressed in HEK293 cells stably expressing GIRK1/2 subunits. Cells were cultured and recorded in dark room conditions after 24 h transfection. GIRK-mediated K^+-currents were measured and analyzed as described previously. The external solution was as follows: 20 mM NaCl, 120 mM KCl, 2 mM $CaCl_2$, 1 mM $MgCl_2$, 10 mM HEPES-KOH, pH 7.3 (KOH). Patch pipettes (3-6 MΩs) were filled with internal solution: 100 mM potassium aspartate, 40 mM KCl, 5 mM MgATP, 10 mM HEPES-KOH, 5 mM NaCl, 2 mM EGTA, 2 mM $MgCl_2$, 0.01 mM GTP, pH 7.3 (KOH). Cells were recorded in external solution containing 1 µM all-*trans* retinal (Sigma). Cells were visualized using a trans-illuminated green light filter (480 nm) during experimental manipulations. Whole-cell patch clamp recordings of HEK293 cells were performed with an EPC9 amplifier (HEKA). Currents were digitized and filtered with the internal 10-kHz three-pole Bessel filter (filter 1) in series with a 2.9-kHz 4-pole Bessel filter (filter 2) of the EPC9 amplifier. Series resistances were partially compensated between 70 and 90%. The Pulse software (HEKA) was used or the controls of voltage and data acquisition, and off-line analysis was made with Igor Pro 6.0 software (Wavemetrics). To identify the wavelength dependency different protocols were established. All protocols were in a range of 380 nm and 690 nm. The light pulses were given in a pseudorandomized order and in increments of 10 from long wavelengths to short wavelengths and conversely. All wavelengths were tested with 10 s light pulses and were deactivated with 30 s of 560 nm. To measure the wavelength dependency for the deactivation 16 wavelengths in a range of 500-650 nm were also tested in a pseudorandomized order and in increments of 10. To ensure the deactivation of melanopsin, a light pulse of 560 nm for 30 s was given after all testing wavelengths. For the measurement of the on and off kinetics 10 s pulses of 450 nm for activation and 30 s of 560 nm for deactivation were given. By an exponential fit τ_{on} and τ_{off} were measured. For the repetitive light activation and deactivation, we applied 20 times 10 s of 450 nm and 30 s of 560 nm. By applying light pulse in a range from 30 ms up to 10 s we could identify the light pulse duration dependency. For the light intensity measurement, we activated the mutant for 1 s with different intensities in a range of 0,015 and 1,5 mW/mm^2. For the relative-self-inactivation the decline of induced GIRK currents during dark phase before deactivation with 560 nm was measured.

AAV2 virus production and stereotactic virus injection

Recombinant AAV stocks of serotype 9 were produced via the triple-transfection method[3] and purified using chloroform. In short, HEK293T cells were transfected with the vector of interest, the serotype plasmid and helper plasmid using polyethylenimine. 72 h after transfection, cells were harvested via low-speed centrifugation. Cells were resuspended in lysis buffer (150 mM NaCl, Tris Cl pH 8.5), freeze-thawed 7 times and incubated with DNaseI plus $MgCl_2$ at 37 °C for 30 min. PEG-8000 (10% final w/v) was added to the supernatant and the mixture incubated for 2 h at 4 °C. After centrifugation at 3,700 x g for 20 min at 4 °C, the PEG-precipitated pellet was resuspended in the clarified cell lysate. For purification, the resuspension was incubated with PEG-8000 for ≥1 h at 4 °C, centrifuged (3700 x g, 4 °C, 20 min), and the pellet resuspended in 50 mM HEPES buffer. Afterwards, room-temperature chloroform (1:1 volume) was added, the mixture vortexed and then spun down at 370 x g at RT for 5 min. The aqueous phase was collected, filtered using a syringe filter (0.22 µm) and concentrated using PEG-8000. The concentrated AAV was resuspended in 1x PBS with 0.001% pluronic F68, aliquoted and stored at -80 °C. For cerebellar *in vivo* and *in vitro* electrophysiological experiments adult wild-type male (C57Bl/6J) mice aged 1-3 months were anesthetized with an initial dose of isoflurane and placed into a stereotaxic frame. Body temperature was controlled with a heating pad and anesthesia was maintained with 1.8-2.0 % isoflurane for the entire session. To prevent corneal drying during surgery the eyes were coated with a moisturizing balm. Animals were sheared from the top of the head and the skin was opened with a sagittal incision along the midline. A burr hole was drilled for virus delivery above the cerebellar vermis (stereotactic coordinates from bregma: -6.5-7 mm anteroposterior (A/P); 0 mm mediolateral (M/L); -2000 dorsoventral (D/V)). A customized glass pipette (tip diameter about 10 µm) attached to a 10 ml syringe was used to deliver AAV solution containing the Y211F mutant via pressure injection in 200 µm steps starting from -2000 µm. After the surgery animals received subcutaneous injections of carprofen (2 mg/kg) for analgesia. Animals were placed individually into their home cages and allowed to recover for at least 7 days before performing electrophysiological experiments.

In vivo extracellular recordings and optical stimulation

For extracellular *in vivo* recordings, anaesthetized mice were placed into a stereotactic frame 7 days after AAV_9 injection. The burr hole from the virus injection was exposed again and the craniotomy was enlarged to a diameter of 1.5 to 2 mm by use of a dental drill. The dura was carefully removed. Extracellular activity was recorded with a multi-electrode system (Eckhorn system, Thomas Recording, Giessen, Germany), and extracellular signals of up to six electrodes (impedance, 2-3 MOhm at 1 kHz; Thomas Recording) were simultaneously amplified and filtered (band-pass, 0.1-8 kHz) with a multichannel signal conditioner (CyerAmp380, Axon Instruments, Union City, CA, USA). All signals were sampled with 32 kHz via an A/D converter (NI PCI-6259 multifunction data acquisition board, National Instruments, Austin, TX, USA) controlled by custommadecustom made software implemented in Matlab (MathWorks, Natick, MA, USA). For light application into the cerebellum a light conducting glass fiber was mounted in the multi-electrode system. A graded index glass fiber with 125 mm diameter cladding and numerical aperture NA = 0.275 (GIF625, ThorLabs, Newton, NJ, USA) was stripped to remove the acrylate coating. The front end of the fiber was commercially heat-pulled and ground (Thomas Recordings, Giessen, Germany) to match the tip geometry of the standard platinum-tungsten electrodes. With an outer diameter of 125 mm, the stripped fiber fits in the 330 mm outer diameter guide tube of the multi-electrode system. The fiber was equipped with a rubber tube and a pulling string similar to the recording electrodes allowing the positioning of the glass fiber in axial direction with similar precision as the electrodes. The upper end of the fiber protruded from the multi-electrode system and was guided through a hole in the lid of the Eckhorn system to a fiber connector for the required adaptations to house the glass fiber in the multi-electrode system. A FC/PC patch cable (ThorLabs) served to connect to a 473 nm diode pumped solid-state (DPSS) laser (BCL-473-020-M, CristaLaser, Reno, NV, USA) with adjustable output power of 20 mW maximum. The laser was gated by a TTL signal provided by the NI multifunction board, which was driven by the Matlab software controlling the data acquisition. When the maximum power of 20 mW was emitted by the laser, a total power in the range of 1.5 to 5 mW was measured in front of the customized fiber tip with a laser power meter (Model 407A, Spectra Physics, Darmstadt, Germany), depending on the particular light fiber used in the experiment. The spatial distribution of light emitted at the pulled and ground tip of the fiber was more strongly dispersed than the light emitted from a fiber with a flat, polished end.

Histology

Mice were deeply anesthetized by an overdosed i.p. injection of ketamine and perfused transcardially with 1 x phosphate-buffered saline (PBS) followed by 4% paraformaldehyde (PFA) in PBS. Brains were removed and post fixed in PFA overnight at 4 °C ensued by tissue immersion in 30% sucrose (w/v) overnight at 4 °C for cryoprotection. Sagittal tissue sections (40 µm) were prepared on a cryostat (Leica CM3050 S) and mounted on Superfrost Plus Microscope Slides and coversliped with Roti®-Mount FluorCare. Fluorescent images were acquired at a Leica TCS SP5 II confocal microscope with 10X/0.3NA, 20X/0.7NA and 40X1.1/NA objectives. Sequential z-stacks were made for each section and transferred to ImageJ software (1.47v; NIH) for processing and image overlay.

Statistics

Statistical significance and numbers of cells, animals and/or trials performed (n) are specified in the figure legends. Statistical significance in all experiments was evaluated using SigmaPlot software (Systat Software) or Igor Pro software (WaveMetrics). For all results, the level of significance was set to $p < 0.05$ and reported as mean ±SEM. Statistical significance is indicated with *** $p < 0.001$; ** $p < 0.01$; * $p < 0.05$.

All experiments were approved by the Institutional Animal Research Facility.

Theoretical Methods

Molecular mechanics simulations

The structure of channelrhodopsin-2 (ChR2, PDB: 6EID[4]) and the Homology model (mouse melanopsin in complex with G_q protein based on PDB-ID 2Z73[5]) was prepared as starting structure for molecular mechanics (MM) simulations in the Moby program suite[6]. We used the ChR2 monomer x-ray structure[4] to update our ChR2 dimer[7,8] with the most recent experimental results[4,9]. Point mutations were introduced employing the Moby program suite[6] including a rotamere search and side chain optimization. Structure preparation included dihedral-, angle-, and bond corrections according to the united atom Amber84 force field[10]. MM simulations were performed according to our previous publications[7–9]. We used the OPLS/AA all atom force field and GROMACS version (2016.3)[11]. All Systems were initially solvated following the Vedani-type[12] and thoroughly solvated in a cubic simulation cell with TIP4P water[13,14] and 154 mM NaCl. Membrane insertion was performed by using lambada[15] (to calculate a hydrophobic belt) and g_membed[11] (to embed the protein in the membrane). Each MM simulation was initiated using a different temperature seed number to generate the random distribution of starting velocities.

Quantum mechanics simulations

Quantum mechanical (QM) excitation energy calculations were carried out using the ONIOM embedded method[16–18] implemented in Gaussian 09[19]. The Moby program suite[6] was employed to prepare the QM input files analogous to our previously published theoretical IR spectroscopy approach[20–22]. We also used the Moby program suite[6] to calculate excitation energies based on the semi empirical MNDOC-CI methods.

Model construction software

The VMD[23] plugin QwikMD[24] was used to set up and conduct interactive molecular dynamics (iMD) simulations and molecular dynamics flexible fitting (MDFF) runs employing NAMD[25] with the CHARMM36 force field[26]. Rosetta[27–29] was used for *ab initio* structure prediction. Modeller[30] was employed for homology modeling. A detailed description of the modeling workflow is given in Supporting Note 2.

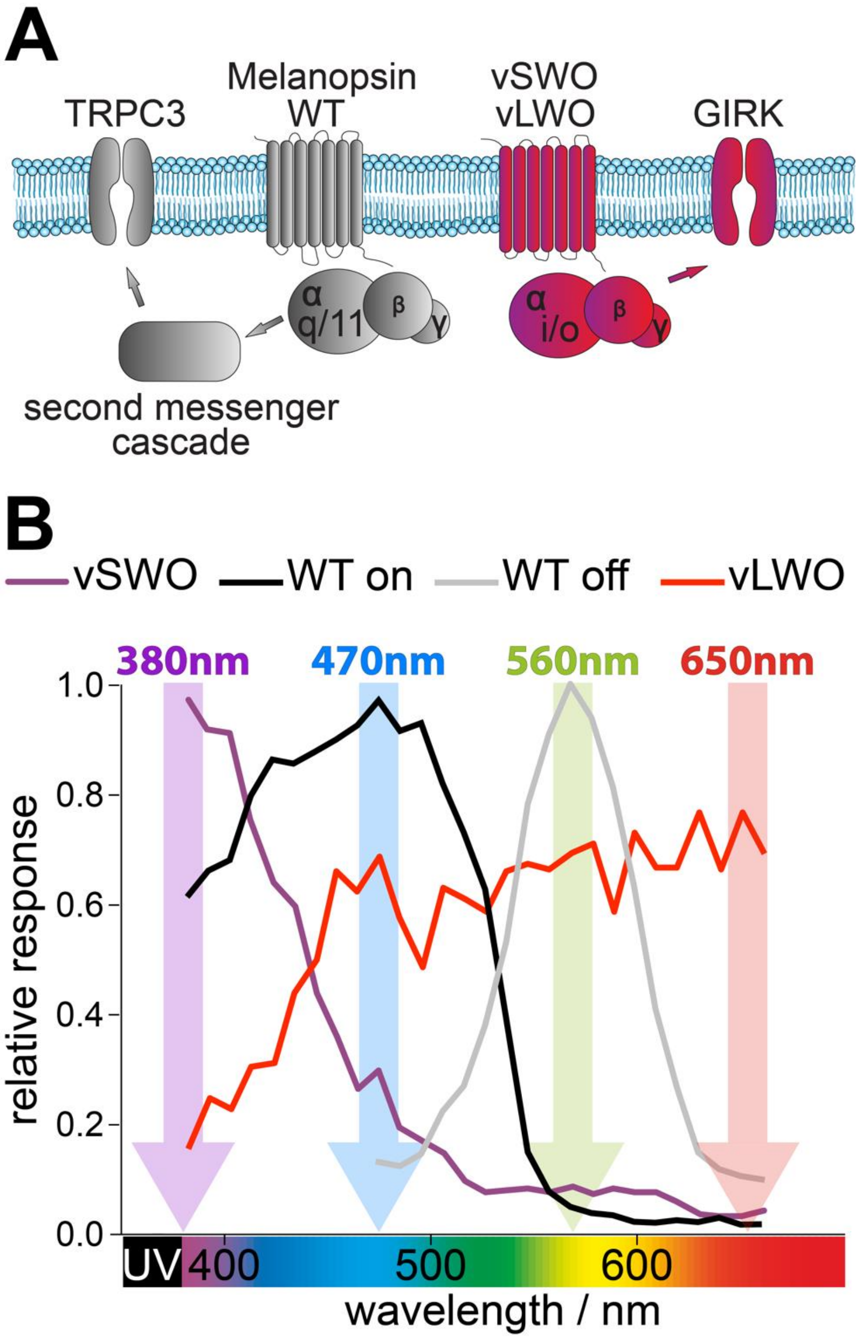

Figure S1: Project motivation. **A** Tandem activation of two different protein pathways by using melanopsin in combination with vLWO or vSWO. **B** Action spectra for activation of vSWO (purple), vLWO (red), Melanopsin WT (black), and for Melanopsin WT deactivation (gray). Each excitation energy is highlighted as arrow colored by the specific wavelength.

Supporting Note 1: Theoretical UV/VIS Spectroscopy

We calculated the excitation energies which result in the theoretical UV/VIS spectra employing DFT based functionals (RCIS=(FC)[31]) and TD[32–38] with the basis sets (6-31G*[39–48]) implemented in Gaussian 09[19]. As QM/MM embedding we used the ONIOM scheme[16–18]. As there is no semi empirical method together with the QM/MM embedding in Gaussian09 available, we used the faster implementation within the MOBY program package[6] to calculate excitation energies based on the semi empirical CI methods MNDOC[49,50] with partial charge of the Amber84 force field[10] with the background charge embedding. The QM fragment contained the cofactor retinal which is bound to the protein via the Schiff base. A link atom was inserted between the Schiff base and the epsilon carbon of the lysine.

For all calculations the QM fragment of the systems contained the cofactor retinal and the Schiff base (N-H). The fixed MM region contained all protein centers, and in addition all lipids, solvent and ion molecules that were within a 4.0 nm shell around the QM fragment. The total charge of the system was always zero. This was achieved by taking Na+/Cl- ions into the MM region that were closest to the QM box.

The workflow is described in Figure S4. For every represent system we calculated 5 independent MM simulations. We used 1001 snapshots of every converged 100 ns MD simulations (snapshot every 0.1 ns).

All ChR2 simulations were calculated as dimer and contained two retinals. From these simulations, the excitation energies of retinal A and B were calculated separately. To determine the UV/VIS spectrum, all single excitation configurations were considered. The resultant excitation energies of one retinal (5 times 1001 excitation energies for the melanopsin systems and 5 times 1001 for Monomer A and 5 times 1001 for Monomer B of the ChR2 systems) were added to a histogram. Melanopsin is a monomer and has only one retinal binding pocket. The obtained histogram for each of the retinal binding pockets consists of in total of 5005 excitation energies. Gnuplot[51] was used to calculate the normal distribution with a bin width of 0.005 eV for the histogram. The maximum value of the normal distribution is the absorption maximum.

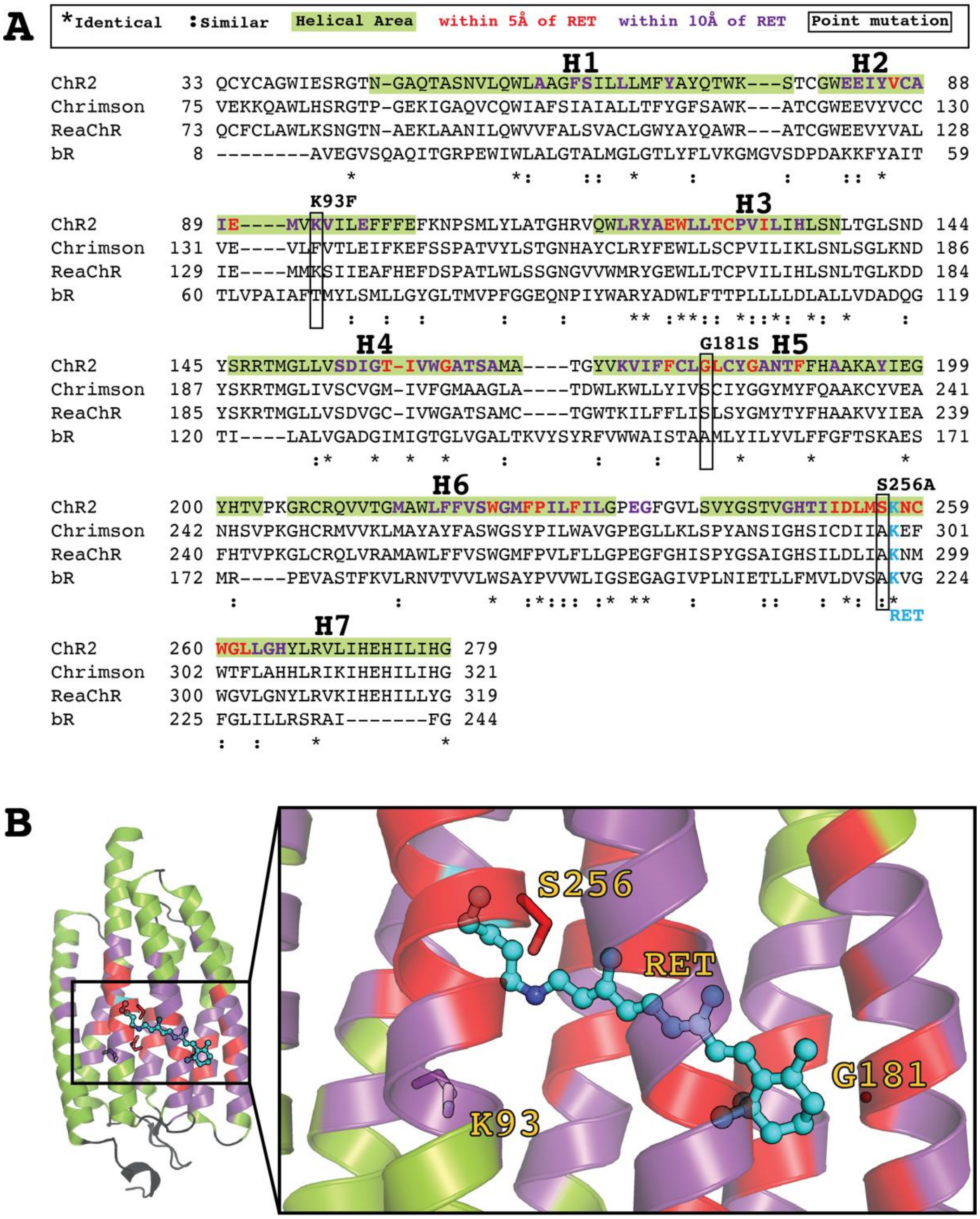

```
                                           H1                       H2
ChR2      33 QCYCAGWIESRGTN-GAQTASNVLQWLAAGFSILLLMFYAYQTWK---STCGWEEIYVCA  88
Chrimson  75 VEKKQAWLHSRGTP-GEKIGAQVCQWIAFSIAIALLTFYGFSAWK---ATCGWEEVYVCC 130
ReaChR    73 QCFCLAWLKSNGTN-AEKLAANILQWVVFALSVACLGWYAYQAWR---ATCGWEEVYVAL 128
bR         8 --------AVEGVSQAQITGRPEWIWLALGTALMGLGTLYFLVKGMGVSDPDAKKFYAIT  59
                        *             *:    ::  *    :       :    :: *

                    K93F                                  H3
ChR2      89 IE----MVKVILEFFFEFKNPSMLYLATGHRVQWLRYAEWLLTCPVILIHLSNLTGLSND 144
Chrimson 131 VE----VLFVTLEIFKEFSSPATVYLSTGNHAYCLRYFEWLLSCPVILIKLSNLSGLKND 186
ReaChR   129 IE----MMKSIIEAFHEFDSPATLWLSSGNGVVWMRYGEWLLTCPVILIHLSNLTGLKDD 184
bR        60 TLVPAIAFTMYLSMLLGYGLTMVPFGGEQNPIYWARYADWLFTTPLLLLDLALLVDADQG 119
                        :  :  :      :    :     ** :**:: *::*: *: *    :

                         H4                          G181S   H5
ChR2     145 YSRRTMGLLVSDIGT-IVWGATSAMA----TGYVKVIFFCLGLCYGANTFFHAAKAYIEG 199
Chrimson 187 YSKRTMGLIVSCVGM-IVFGMAAGLA----TDWLKWLLYIVSCIYGGYMYFQAAKCYVEA 241
ReaChR   185 YSKRTMGLLVSDVGC-IVWGATSAMC----TGWTKILFFLISLSYGMYTYFHAAKVYIEA 239
bR       120 TI----LALVGADGIMIGTGLVGALTKVYSYRFVWWAISTAAMLYILYVLFFGFTSKAES 171
                     :*   *  *  *    :       :    :      *     *       *

                                H6                                   S256A
ChR2     200 YHTVPKGRCRQVVTGMAWLFFVSWGMFPILFILGPEGFGVLSVYGSTVGHTIIDLMSKNC 259
Chrimson 242 NHSVPKGHCRMVVKLMAYAYFASWGSYPILWAVGPEGLLKLSPYANSIGHSICDIIAKEF 301
ReaChR   240 FHTVPKGLCRQLVRAMAWLFFVSWGMFPVLFLLGPEGFGHISPYGSAIGHSILDLIAKNM 299
bR       172 MR----PEVASTFKVLRNVTVVLWSAYPVVWLIGSEGAGIVPLNIETLLFMVLDVSAKVG 224
              :             :       *  :*::: :* **   :     ::   : *: :*
                                                                      RET

                      H7
ChR2     260 WGLLGHYLRVLIHEHILIHG 279
Chrimson 302 WTFLAHHLRIKIHEHILIHG 321
ReaChR   300 WGVLGNYLRVKIHEHILLYG 319
bR       225 FGLILLRSRAI-------FG 244
             :  :    *          *
```

Figure S2: Sequence alignment of several microbial rhodopsins and positions of identified variants for color tuning. **A** A Sequence alignment of ChR2 with Chrimson[52], ReaChR[53] and bR[54] are shown. The Area 10 Å around the Retinal is colored purple and 5 Å around the retinal is colored red. **B** ChR2 overview (left) and ChR2 retinal binding pocket (right) based on the ChR2 crystal structure[4]. Helices are shown in green and the respective positions of the variants are shown in sticks. The all-*trans* retinal is shown in cyan. The orbits around the retinal are colored as in A.

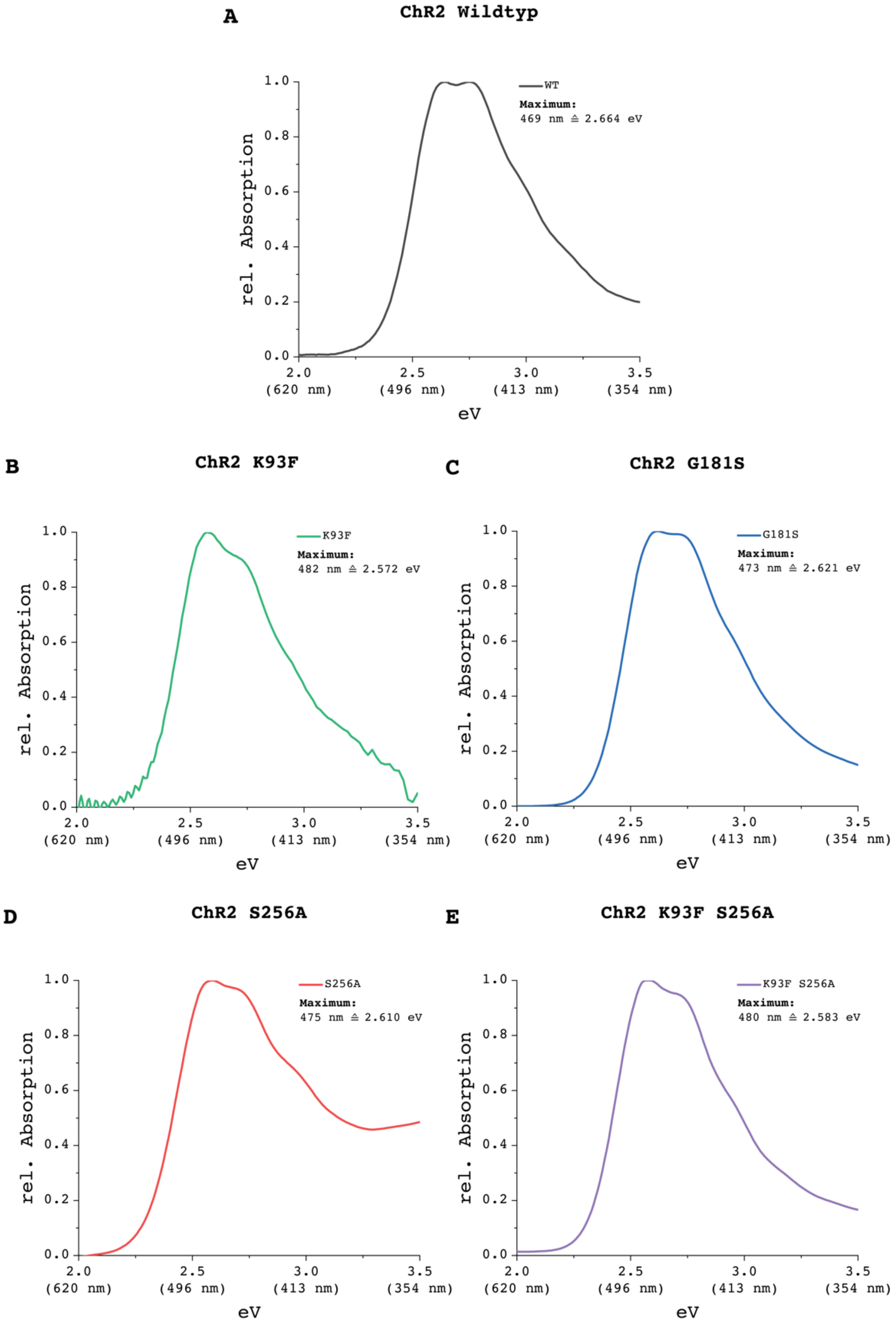

Figure S3: UV/VIS measurements of channel rhodopsin mutants. All Absorption spectra are normed to 1 and given in eV for comparability to the calculated values. The measured maxima are given beside the respective spectrum.

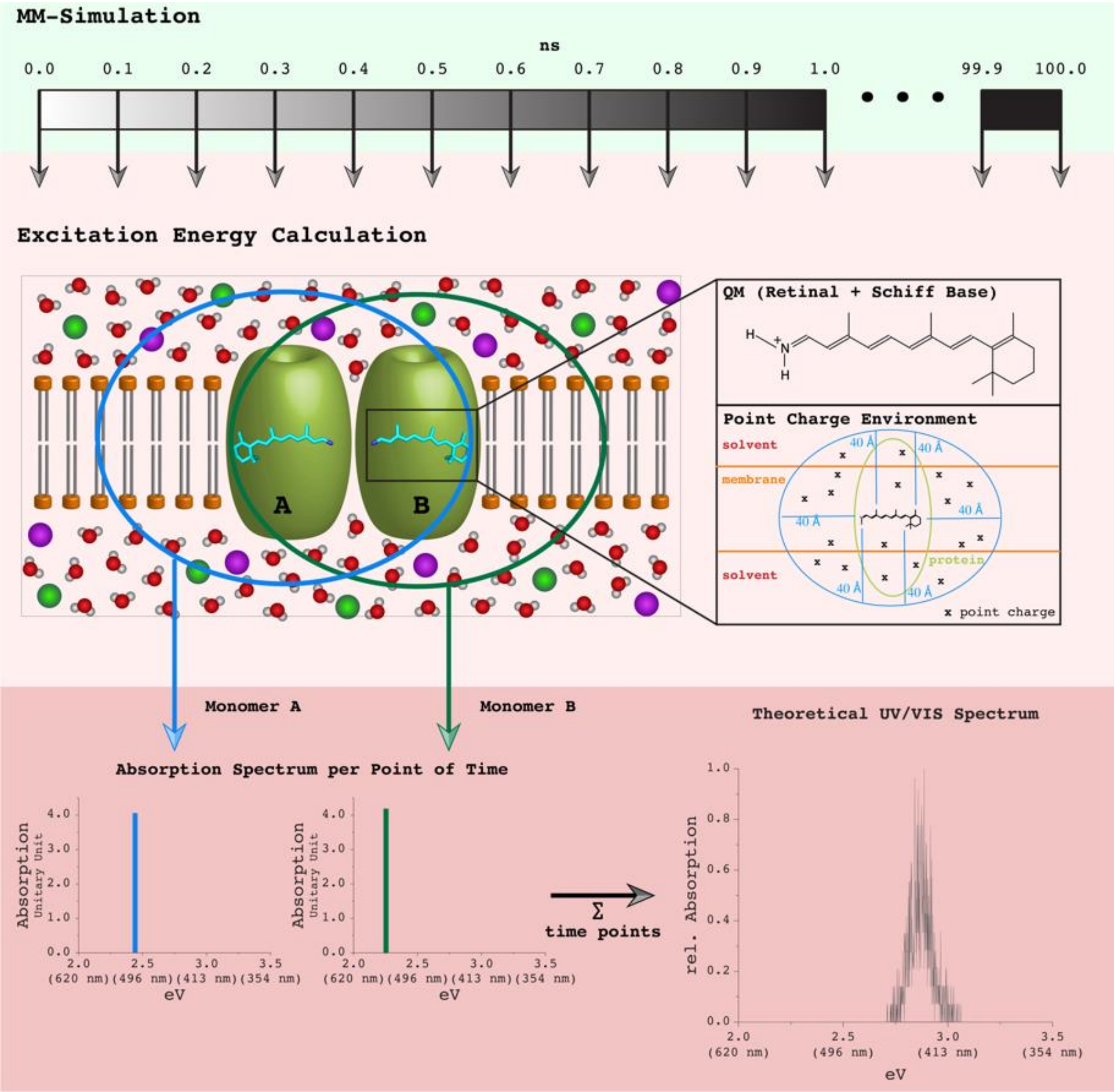

Figure S4: Theoretical UV-VIS spectroscopy workflow. For every represent system we calculated 5 independent MD simulations and used 1001 snapshots of every converged 100 ns MD simulations (snapshot every 0.1 ns). We calculate the excitation energy by using the ONIOM embedded method[16–18]. The QM fragment of the systems contained the cofactor retinal and the Schiff base (N-H). The fixed MM region contained all protein centers, and in addition all Lipids, solvent and ion molecules that were within a 4.0 nm shell around the QM fragment. We calculated the excitation energy with MNDOC[49,50], TD[32–38] and the RCIS=(FC)[31] Methods. For TD and RCIS=(FC) we used the basis sets 6-31G*[39–48]. To determine the UV/VIS spectrum, all excitation energies of one system were added to a histogram. After this the normal distribution with a range of 0.005 eV was calculated. The maximum value of the normal distribution is the absorption maximum.

Supporting Table 1: **UV/VIS absorption maxima.** The absorption maxima are given in eV.

	measured	MNDOC	TD/6-31G*	RCIS=(FC)/6-31G*
ChR2 WT	2.644	2.723	3.031	3.230
ChR2 G181S	2.621	2.704	3.001	3.200
ChR2 S256A	2.611	2.684	2.993	3.193
ChR2 K93F	2.572	2.680	3.002	3.200
ChR2 K93F S256A	2.583	2.674	2.988	3.188
Melanopsin WT	2.638	2.414	-	-
Melanopsin Y211F	2.755	2.430	-	-

Supporting Note 2: Model construction and validation

We used our recently developed hybrid modeling workflow combining homology modeling with *ab initio* structure prediction[55–58] to generate a homology model of mouse melanopsin (UNIPROT-ID Q9QXZ9). The basis for the model is the squid rhodopsin crystal structure (PDB-ID 2Z73[5]). The low sequence similarity in the helical areas of approx. 55% (identity 33%) demanded various optimisation steps: We incorporated additional information about helical membrane domains (identified using secondary structure prediction with Rosetta[27–29] and constrained consensus topology prediction server (CCTOP)[59] and conserved functional elements that are known from other Opsins like Glucagon-like peptide1 receptor (PDB-ID 5VAI[60]), Calcitonin receptor (PDB-ID 5UZ7[61]), Beta-2 adrenergic receptor (PDB-ID 3SN6[62]), Bos taurus Rhodopsin (PDB-ID 3DQB[63]), Squid rhodopsin (PDB-ID 2Z73[5]) as shown in Figure S6.

Within the iterative process that involves Monte Carlo based (Rosetta[27–29] and MD based structure optimization (Moby-program package[6]) the model is solvated, placed into the membrane and optimised regarding, side chain orientation, and hydrogen bond network. Then the model is equilibrated by MM simulations (Gromacs[11]) to adapt to its physiological environment. The key functional region, the retinal binding pocket, contains highly conserved functionally relevant amino acids. The sequence similarity for the amino acids in a distance of 5 Å around the retinal between mouse melanopsin and the squid rhodopsin crystal structure is 79% (identity 51%) (Supporting Table 2). Further conserved anchor points in helix-2, helix-3, helix-4, helix-5, helix-6, and helix-7 result from a multiple sequence alignment of various opsins[5,60–63] (Figure 2). Based on these values we expect a highly accurate homology model for the retinal binding pocket.

For the calculation of the UV/VIS spectra we needed a homology model of mouse melanopsin in complex with the human G_q protein. For the models we used the β_2AR crystal structure (PDB-ID 3SN6[62]). We replaced the β_2AR structure by the above built melanopsin model. The $G\alpha_s$ and Gɣ from bovine as well as the rat Gβ are used as template to build a homology model for the human G_q protein ($G\alpha_q$ (UNIPROT-ID P50148) with Gβ (UNIPROT-ID P62873-2) and Gɣ (UNIPROT-ID G3V2N0)). The three alignments are shown in Supporting Figures S7 and S8. As helix 5 and 6 from melanopsin clash with the Gα subunit we used QwikMD[64] to run an interactive molecular dynamics simulation calling NAMD[25] through VMD[23] to move these two helices outwards. We assume that the overall shape between the β2AR and the G_s protein is highly similar to the shape of the melanopsin G_q protein complex. Therefore, we refined the melanopsin G-protein complex to the shape of β2AR using molecular dynamics flexible fitting (MDFF) simulations[65]. The x-ray structure of β2AR (PDB-ID 3SN6)[62] was converted into a volumetric density using volutiles of VMD[23]. QwikMD[24] was used to set up and conduct MDFF runs employing NAMD[25] with the CHARMM36 force field[26].

Sekharan et al.[66] published a melanopsin crystal structure in 2012 based on the same template as we used namely squid rhodopsin (PDB ID 2Z73[5]). However, the model from Sekharan et al. has a severe flaw as they erroneously introduced a non-existing extra isoleucine residue at position 129 into the mouse melanopsin sequence (UNIPROT ID Q9QXZ9). We also note that Sekharan et al.[66] only employed secondary structure prediction by TMHMM[67] which predicts only six transmembrane helices (Supporting Figure S4) for a seven transmembrane helical protein. This underlines that for a reasonable guess of the secondary structure of heptahelical transmembrane proteins the combination of several prediction tools is necessary. For these reasons, we do not used the model of Sekharan et al.[66].

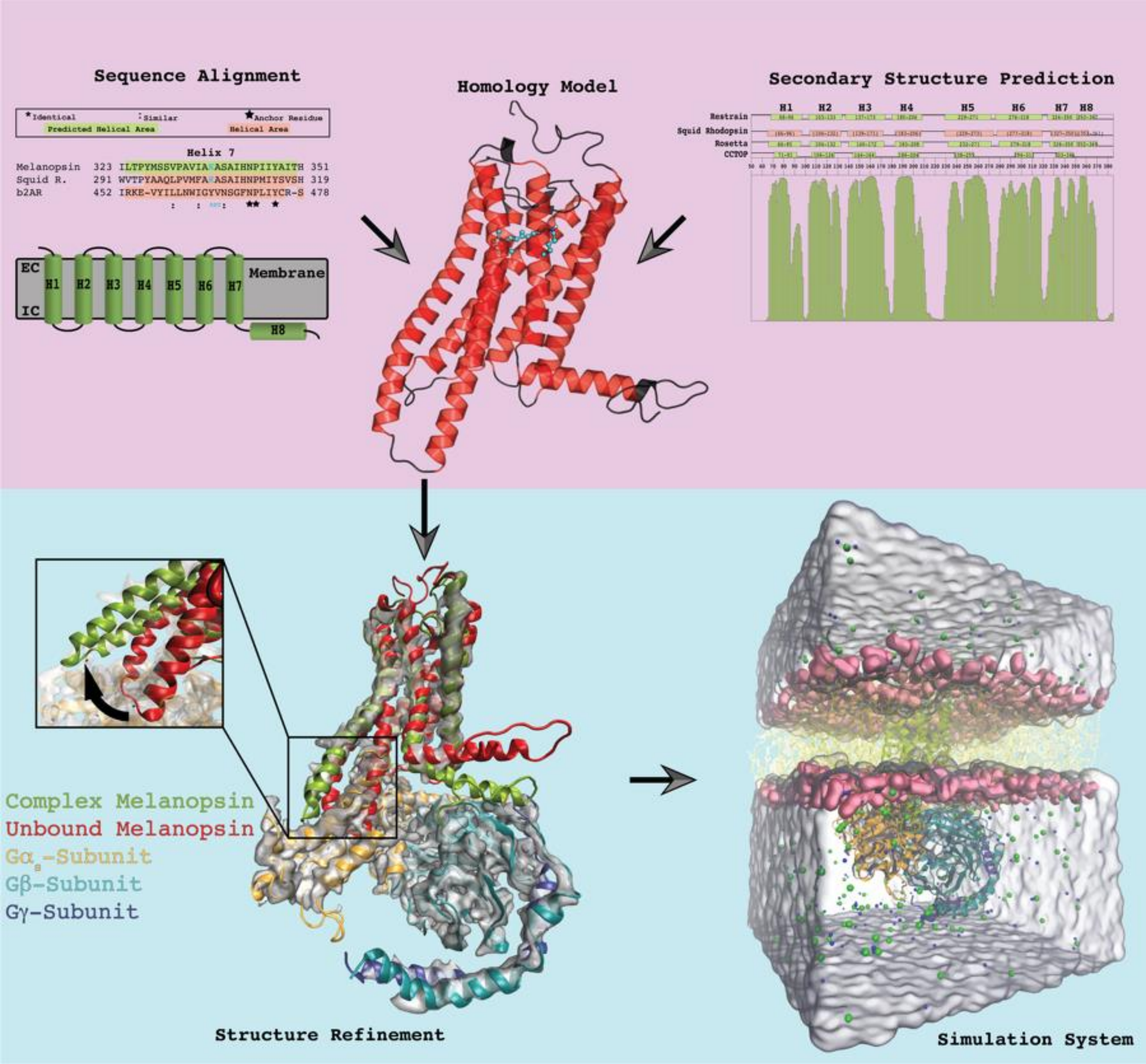

Figure S5: Hybrid modeling workflow to construct the melanopsin G_q protein complex. The top panel (light red) shows the process of homology modeling of unbound mouse melanopsin (red structure) with Modeller[30]. First, the optimal template and sequence alignment was identified using ClustalOmega[68]. For the here used data see Figure 2. Simultaneously, the secondary structure was estimated using the meta server CCTOP[59] and *ab inito* structure prediction employing Rosetta[27–29]. For the here used data see Supporting Figure S5. The same process was repeated to build the homology models of the three human G_q protein subunits. Second, the melanopsin G protein complex is build using molecular dynamics flexible fitting[65] to refine the structure to an artificial density of the related β_2AR crystal structure (PDB-ID 3SN6[62]). Last, the mouse melanopsin human G_q protein complex is solvated and embedded in a membrane. In order to equilibrate the system to its physiological environment a molecular mechanics simulation is performed.

Supporting Table 2: **Sequence identity and similarity of mouse melanopsin and squid rhodopsin**. Data are given in %.

%	All	No Ter	RET 5Å	RET 10Å	H1-8	H1	H2	H3	H4	H5	H6	H7	H8
Identity	33	41	45	51	40	41	50	40	39	31	33	56	39
Similarity	55	68	72	79	68	59	72	69	77	53	69	88	61

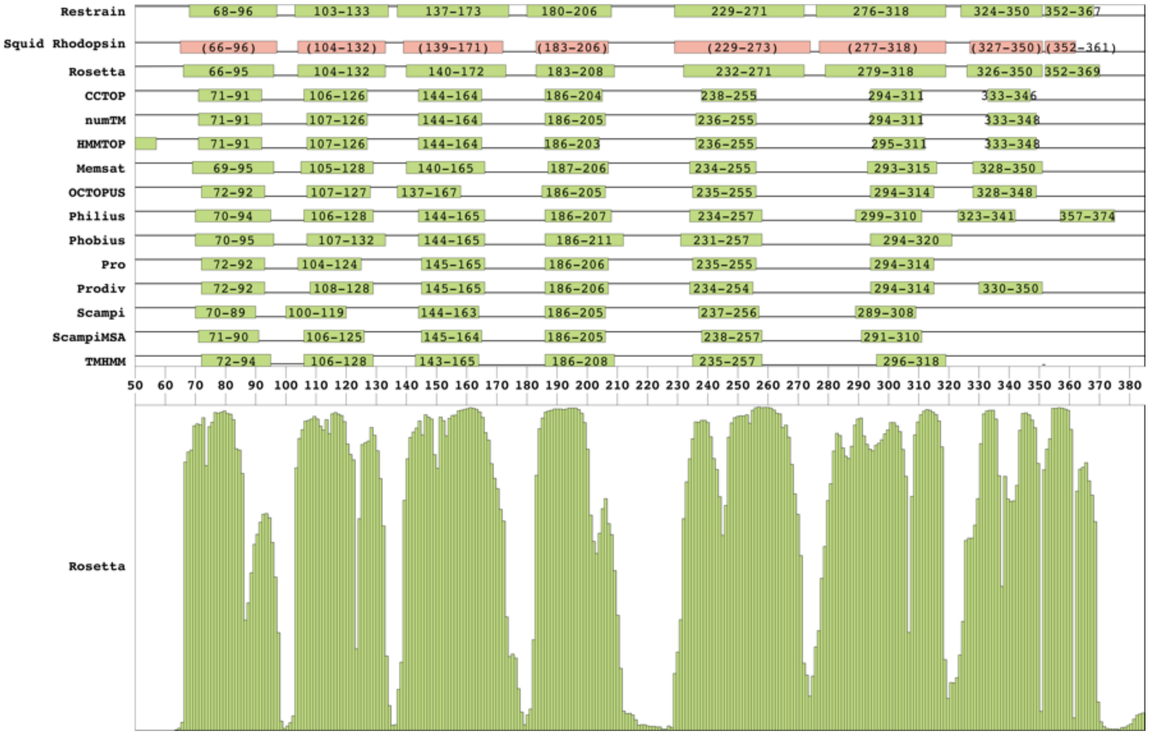

Figure S6: CCTOP and Rosetta secondary structure prediction. The top illustrates the CCTOP results of the secondary structure prediction for mouse melanopsin and the bottom represents the results of the rosetta secondary structure prediction for the same template. All results were merged and included as restrains in the calculation of the homology model. The helical area of the squid rhodopsin crystal structure (PDB-ID 2Z73[5]) is colored in light red.

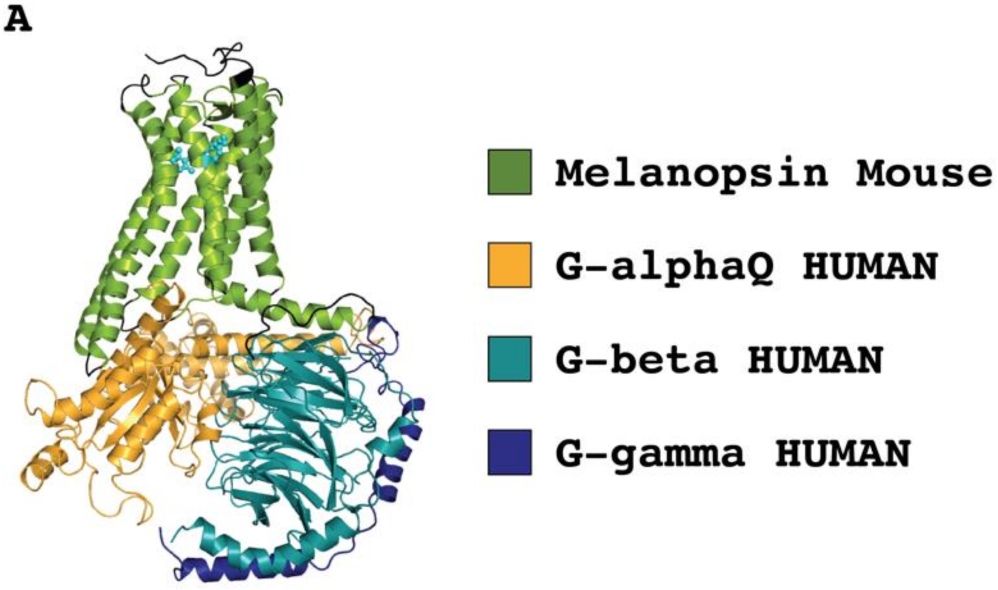

B G-alphaQ

```
                     *Identical: 42 %                          :Similar: 67 %

G-alphaS BOVINE   1   ------MGCLGNSKTEDQRNEEKAQREANKKIEKQLQKDKQVYRATHRLLLLGAGESGKS   54
G-alphaQ HUMAN    1   MTLESIMACCLS-------EEAKEARRINDEIERQLRRDKRDARRELKLLLLGTGESGKS   53
                            * *          :* *  *  * :**:**::**:  *   :*****:******

G-alphaS BOVINE   55  TIVKQMRILHVNGFNGDSEKATKVQDIKNNLKEAIETIVAAMSNLVPPVELANPENQFRV   114
G-alphaQ HUMAN    54  TFIKQMRIIHGSGYSDEDKRGFTKL-VYQNIFTAMQAMIRAMDTLKIPYKYEHNKAHAQL   112
                      *::*****:*  *:  : ::      : :*:  *::::: **  *  * :  : : : ::

G-alphaS BOVINE   115 DYILSVMNVPDFDFPPEFYEHAKALWEDEGVRACYERSNEYQLIDCAQYFLDKIDVIKQD   174
G-alphaQ HUMAN    113 VREVDVEKV--SAFENPYVDAIKSLWNDPGIQECYDRRREYQLSDSTKYYLNDLDRVADP   170
                         : * :*    *   : :  *:**:* *:: **:*  **** * ::*:*: :* : :

G-alphaS BOVINE   175 DYVPSDQDLLRCRVLTSGIFETKFQVDKVNFHMFDVGGQRDERRKWIQCFNDVTAIIFVV   234
G-alphaQ HUMAN    171 AYLPTQQDVLRVRVPTTGIIEYPFDLQSVIFRMVDVGGQRSERRKWIHCFENVTSIMFLV   230
                       *:*::**:** ** *:**:*  *::: * *:* ****** ******:**::**:*:*:*

G-alphaS BOVINE   235 ASSSYNMVIREDNQTNRLQEALNLFKSIWNNRWLRTISVILFLNKQDLLAEKVLAGKSKI   294
G-alphaQ HUMAN    231 ALSEYDQVLVESDNENRMEESKALFRTIITYPWFQNSSVILFLNKKDLLEEKIMY--SHL   288
                      * * *: *: * :: **::*:  **::*    *::  ********:*** **::   *::

G-alphaS BOVINE   295 EDYFPEFARYTTPEDATPEPGEDPRVTRAKYFIRDEFLRISTASGDGRHYCYPHFTCAVD   354
G-alphaQ HUMAN    289 VDYFPEYDGPQRD------------AQAAREFILKMFVDL---NPDSDKIIYSHFTCATD   333
                       *****:                     *: **   *: :     *  :  * ***** *

G-alphaS BOVINE   355 TENIRRVFNDCRDIIQRMHLRQYELL  380
G-alphaQ HUMAN    334 TENIRFVFAAVKDTILQLNLKEYNLV  359
                      ***** **   :* * :::*::*:*:
```

Figure S7: Illustration of the mouse melanopsin homology model and sequence alignment. **A** Shown is the mouse melanopsin homology model in complex with the G_q protein. **B** Represented is the sequence alignment between $G\alpha_s$ bovine (PDB-ID: 3SN6[62]) and $G\alpha_q$ human (UNIPROT-ID: P50148).

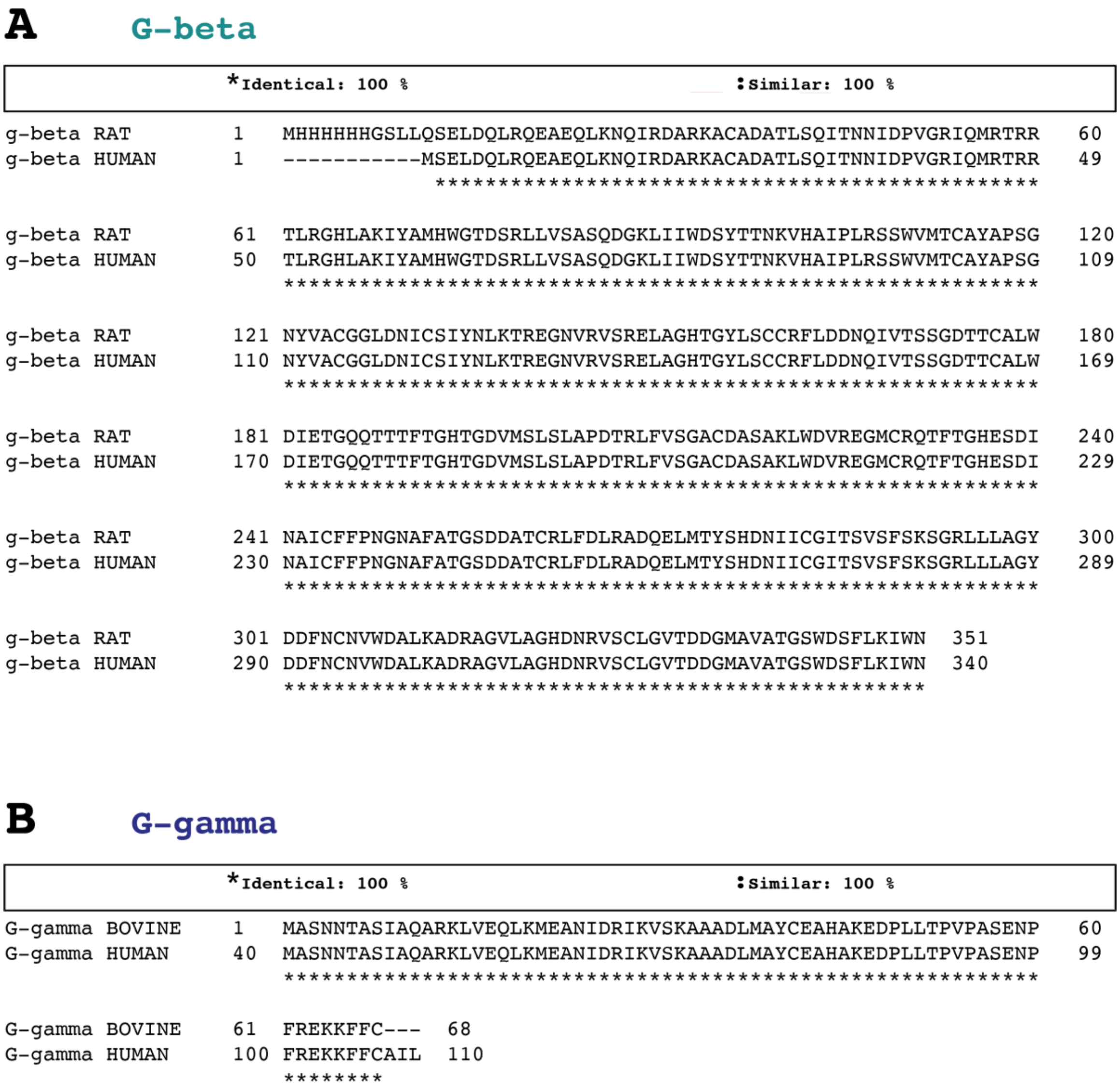

A G-beta

```
                      *Identical: 100 %                        :Similar: 100 %

g-beta RAT        1   MHHHHHHGSLLQSELDQLRQEAEQLKNQIRDARKACADATLSQITNNIDPVGRIQMRTRR   60
g-beta HUMAN      1   -----------MSELDQLRQEAEQLKNQIRDARKACADATLSQITNNIDPVGRIQMRTRR   49
                                 *************************************************

g-beta RAT        61  TLRGHLAKIYAMHWGTDSRLLVSASQDGKLIIWDSYTTNKVHAIPLRSSWVMTCAYAPSG   120
g-beta HUMAN      50  TLRGHLAKIYAMHWGTDSRLLVSASQDGKLIIWDSYTTNKVHAIPLRSSWVMTCAYAPSG   109
                      ************************************************************

g-beta RAT        121 NYVACGGLDNICSIYNLKTREGNVRVSRELAGHTGYLSCCRFLDDNQIVTSSGDTTCALW   180
g-beta HUMAN      110 NYVACGGLDNICSIYNLKTREGNVRVSRELAGHTGYLSCCRFLDDNQIVTSSGDTTCALW   169
                      ************************************************************

g-beta RAT        181 DIETGQQTTTFTGHTGDVMSLSLAPDTRLFVSGACDASAKLWDVREGMCRQTFTGHESDI   240
g-beta HUMAN      170 DIETGQQTTTFTGHTGDVMSLSLAPDTRLFVSGACDASAKLWDVREGMCRQTFTGHESDI   229
                      ************************************************************

g-beta RAT        241 NAICFFPNGNAFATGSDDATCRLFDLRADQELMTYSHDNIICGITSVSFSKSGRLLLAGY   300
g-beta HUMAN      230 NAICFFPNGNAFATGSDDATCRLFDLRADQELMTYSHDNIICGITSVSFSKSGRLLLAGY   289
                      ************************************************************

g-beta RAT        301 DDFNCNVWDALKADRAGVLAGHDNRVSCLGVTDDGMAVATGSWDSFLKIWN  351
g-beta HUMAN      290 DDFNCNVWDALKADRAGVLAGHDNRVSCLGVTDDGMAVATGSWDSFLKIWN  340
                      ***************************************************
```

B G-gamma

```
                      *Identical: 100 %                        :Similar: 100 %

G-gamma BOVINE    1   MASNNTASIAQARKLVEQLKMEANIDRIKVSKAAADLMAYCEAHAKEDPLLTPVPASENP   60
G-gamma HUMAN     40  MASNNTASIAQARKLVEQLKMEANIDRIKVSKAAADLMAYCEAHAKEDPLLTPVPASENP   99
                      ************************************************************

G-gamma BOVINE    61  FREKKFFC---  68
G-gamma HUMAN     100 FREKKFFCAIL  110
                      ********
```

Figure S8: Sequence alignment of Gβ and Gγ. **A** Shown is the sequence alignment between Gβ rat (PDB-ID 3SN6[62]) and Gβ human (UNIPROT-ID: P62873-2). **B** The sequence alignment between Gγ bovine (PDB-ID 3SN6[62]) and Gγ human (UNIPROT-ID: G3V2N0) is represented.

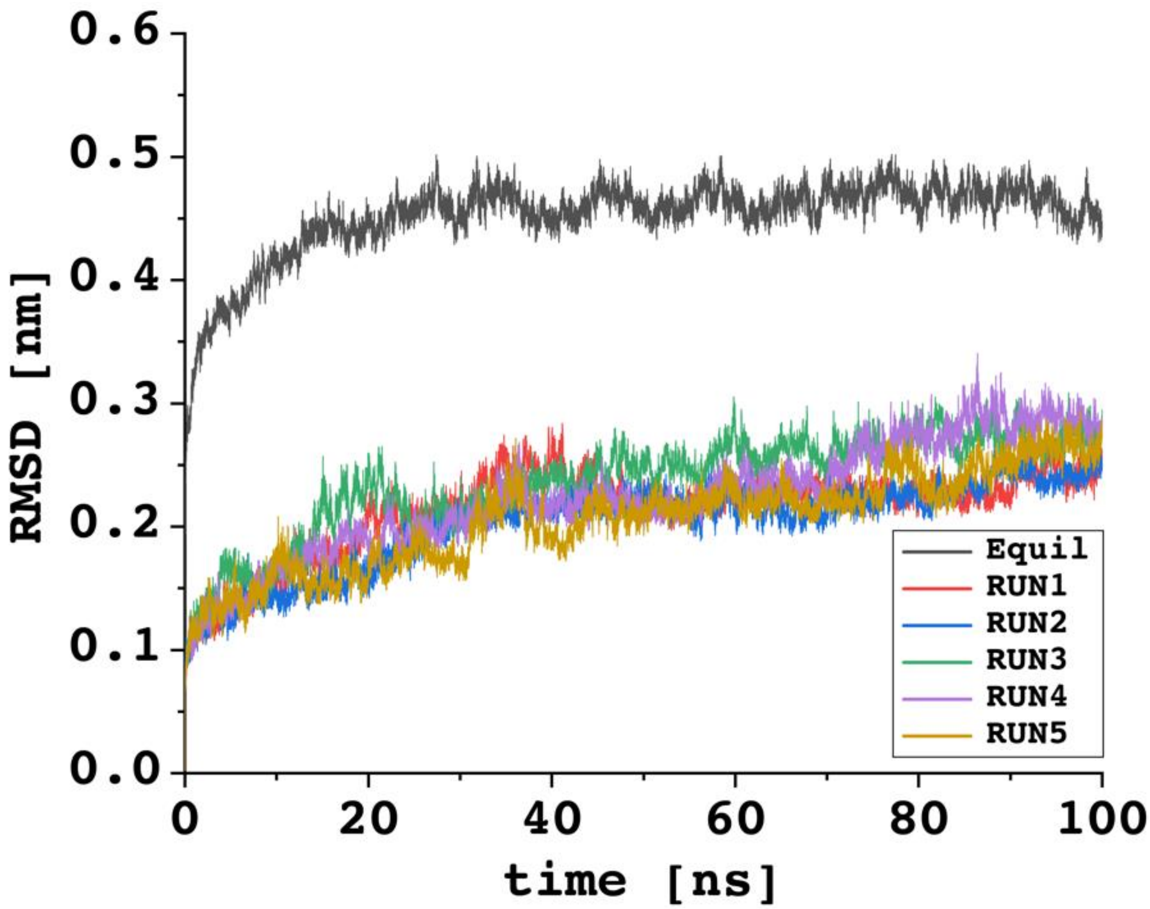

Figure S9: RMSD of the MM simulations based on our constructed mouse melanopsin G_q protein complex. Shown is the RMSD of the equilibration and the subsequent 5 independent production MM simulations. All 5 production runs are stable.

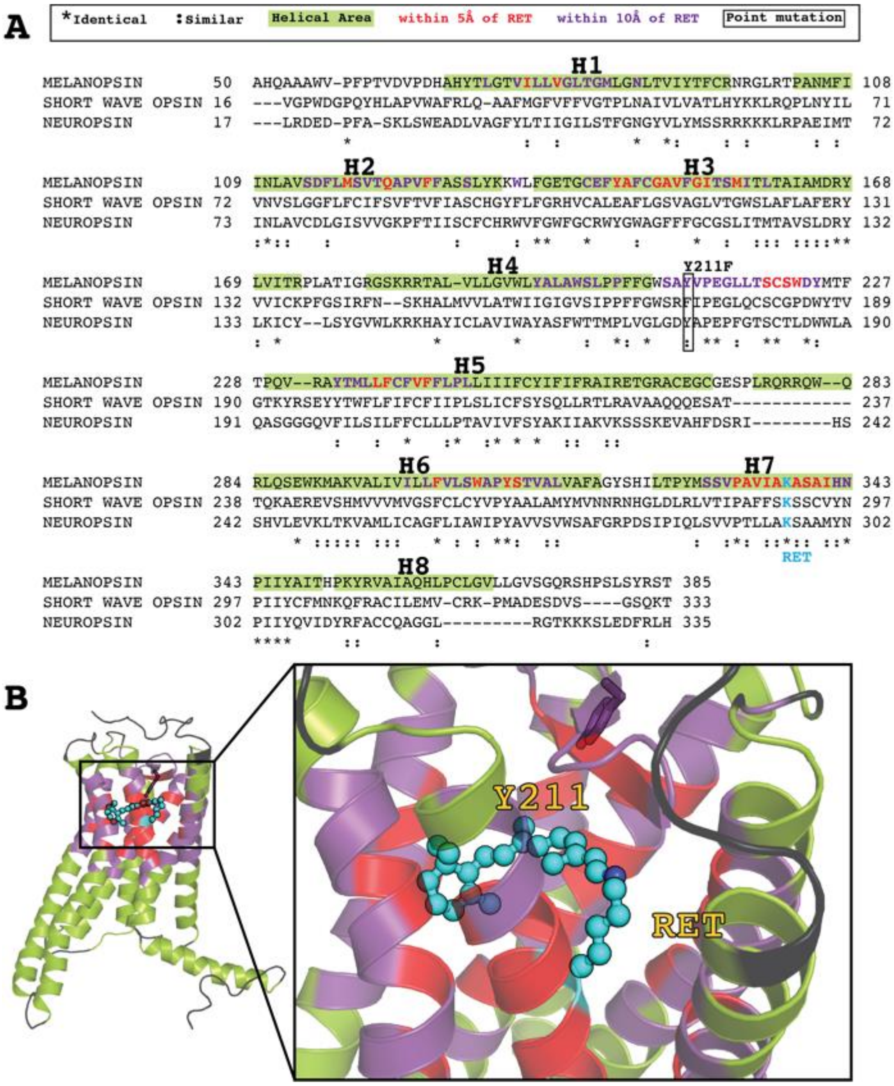

```
                                                        H1
MELANOPSIN       50  AHQAAAWV-PFPTVDVPDHAHYTLGTVILLVGLTGMLGNLTVIYTFCRNRGLRTPANMFI 108
SHORT WAVE OPSIN 16  ---VGPWDGPQYHLAPVWAFRLQ-AAFMGFVFFVGTPLNAIVLVATLHYKKLRQPLNYIL  71
NEUROPSIN        17  ---LRDED-PFA-SKLSWEADLVAGFYLTIIGILSTFGNGYVLYMSSRRKKKLRPAEIMT  72
                              *                 :  :       *  *:    : :      : :

                               H2                                 H3
MELANOPSIN       109 INLAVSDFLMSVTQAPVFFASSLYKKWLFGETGCEFYAFCGAVFGITSMITLTAIAMDRY 168
SHORT WAVE OPSIN 72  VNVSLGGFLFCIFSVFTVFIASCHGYFLFGRHVCALEAFLGSVAGLVTGWSLAFLAFERY 131
NEUROPSIN        73  INLAVCDLGISVVGKPFTIISCFCHRWVFGWFGCRWYGWAGFFFGCGSLITMTAVSLDRY 132
                     :*::   :            :     : **   *    :     *  :  ::: ::::**

                                          H4                Y211F
MELANOPSIN       169 LVITRPLATIGRGSKRRTAL-VLLGVWLYALAWSLPPFFGWSAYVPEGLLTSCSWDYMTF 227
SHORT WAVE OPSIN 132 VVICKPFGSIRFN--SKHALMVVLATWIIGIGVSIPPFFGWSRFIPEGLQCSCGPDWYTV 189
NEUROPSIN        133 LKICY--LSYGVWLKRKHAYICLAVIWAYASFWTTMPLVGLGDYAPEPFGTSCTLDWWLA 190
                     : *               *       *      :  *: *   : ** :  **  *:

                                       H5
MELANOPSIN       228 TPQV--RAYTMLLFCFVFFLPLLIIIFCYIFIFRAIRETGRACEGCGESPLRQRRQW--Q 283
SHORT WAVE OPSIN 190 GTKYRSEYYTWFLFIFCFIIPLSLICFSYSQLLRTLRAVAAQQQESAT------------ 237
NEUROPSIN        191 QASGGGQVFILSILFFCLLLPTAVIVFSYAKIIAKVKSSSKEVAHFDSRI--------HS 242
                             :   :  *   :*  :* * *  ::  ::

                                     H6                                 H7
MELANOPSIN       284 RLQSEWKMAKVALIVILLFVLSWAPYSTVALVAFAGYSHILTPYMSSVPAVIAKASAIHN 343
SHORT WAVE OPSIN 238 TQKAEREVSHMVVVMVGSFCLCYVPYAALAMYMVNNRNHGLDLRLVTIPAFFSKSSCVYN 297
NEUROPSIN        242 SHVLEVKLTKVAMLICAGFLIAWIPYAVVSVWSAFGRPDSIPIQLSVVPTLLAKSAAMYN 302
                         * ::::: :::   * : : **:  ::             :  :*: ::*:: ::*
                                                                          RET

                                     H8
MELANOPSIN       343 PIIYAITHPKYRVAIAQHLPCLGVLLGVSGQRSHPSLSYRST 385
SHORT WAVE OPSIN 297 PIIYCFMNKQFRACILEMV-CRK-PMADESDVS----GSQKT 333
NEUROPSIN        302 PIIYQVIDYRFACCQAGGL---------RGTKKKSLEDFRLH 335
                     ****     ::       :                    :
```

Figure S10: Sequence alignment of several opsins and positions of an identified mutant for color tuning. **A** A sequence alignment of melanopsin with short-wave opsin[69] and neuropsin[70] is shown. The Area 10 Å around the Retinal is colored purple and 5 Å around the retinal is colored red. **B** Melanopsin overview (left) and melanopsin retinal binding pocket (right) based on the established homology model. Helices are shown in green and the respective point mutations are shown in sticks. The all-*trans* retinal is shown in cyan. The orbits around the retinal are colored as in A.

Supporting Note 3: UV/VIS and action spectra comparison

The λ_{max} obtained through electrophysiology and UV/VIS spectroscopy is about the same even though the overall shape might vary, e.g. depending on the light intensity. I. e. the obtained λ_{max} for ChR2 by electrophysiology is 470 nm (2.638 eV)[71] compared to λ_{max} 469 nm (2.644 eV) by UV/VIS spectroscopy.

Supporting Note 4:
Electrophysiological characterization of the Y211F melanopsin variant

For detailed biophysical characterization of the Y211F melanopsin mutant patch-clamp recordings of light-induced GIRK1,2 currents expressed in HEK293 cells were performed [2,69,72].

We first analyzed the light-pulse duration and light-intensity dependence of Y211F induced GIRK currents. As shown in Figure S15A, we found that a ≥200 ms long light pulse is sufficient to induce maximal GIRK current amplitudes. In optogenetic experiments *in vivo* we routinely use 1 s light-pulses (see example patch-clamp trace Figure S12A). The light intensity which has to be used to induce maximal GIRK current amplitudes using a 1 s light pulse is around >0.06 mW/mm^2 (Figure S15B). Since Y211F mutant has faster τ_{on} and τ_{off} kinetics in comparison to wt melanopsin we can conclude that our mutant allows for fast temporal precision of GPCR pathway activation with low phototoxicity in optogenetic applications.

Y211F melanopsin exhibits a decline in light-induced GIRK currents during long-term activation. (Figure 3 and Figure S12B) In order to analyze this further we applied light pulses with different durations. We performed measurements with 1 s, 5 s and 10 s light activation followed by a 30 s dark phase before deactivating Y211F with a 30 s 560 nm long light pulse (Figure S12A). The experiments reveal that increasing light pulse duration increases the decline Y211F induced GIRK currents (Figure S12B).

The direct comparison of the relative current decline between WT and mutant melanopsin reveales that the light-induced GIRK current after 10 s light pulse declines to 45% for Y211F and to 15% for WT (Figure S12B). The decline in response amplitude is also observed for the $G_{q/11}$ induced Y211F mediated intracellular Ca^{2+} responses (Figure S14A).

Since Y211F reveals very fast activation and deactivation kinetics in comparison to other GPCRs we next tested if light activation pulses followed by immediate deactivation light pulses allows for repetitive G protein activation without decline in response amplitude. In fact 10 s 450 nm light pulses followed by 30 sec 560 nm deactivation light pulses can be used to repetitively activate G protein signals without decline in response amplitude (Figure S13).

The wavelength dependence of deactivation reveals a λ_{max} of 560 nm (Figure S11), which is comparable to the wavelength dependence of deactivation of WT melanopsin[2].

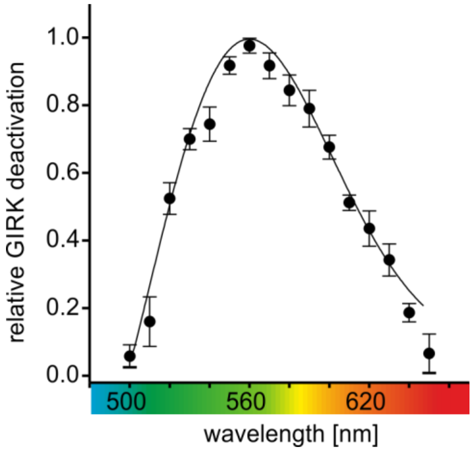

Figure S11: Wavelength dependent deactivation of GIRK currents in HEK293 cells of Y211F. Relative light induced GIRK current deactivation, 10 s of 450 nm light pulse activation, followed by 30 s light dependent deactivation.

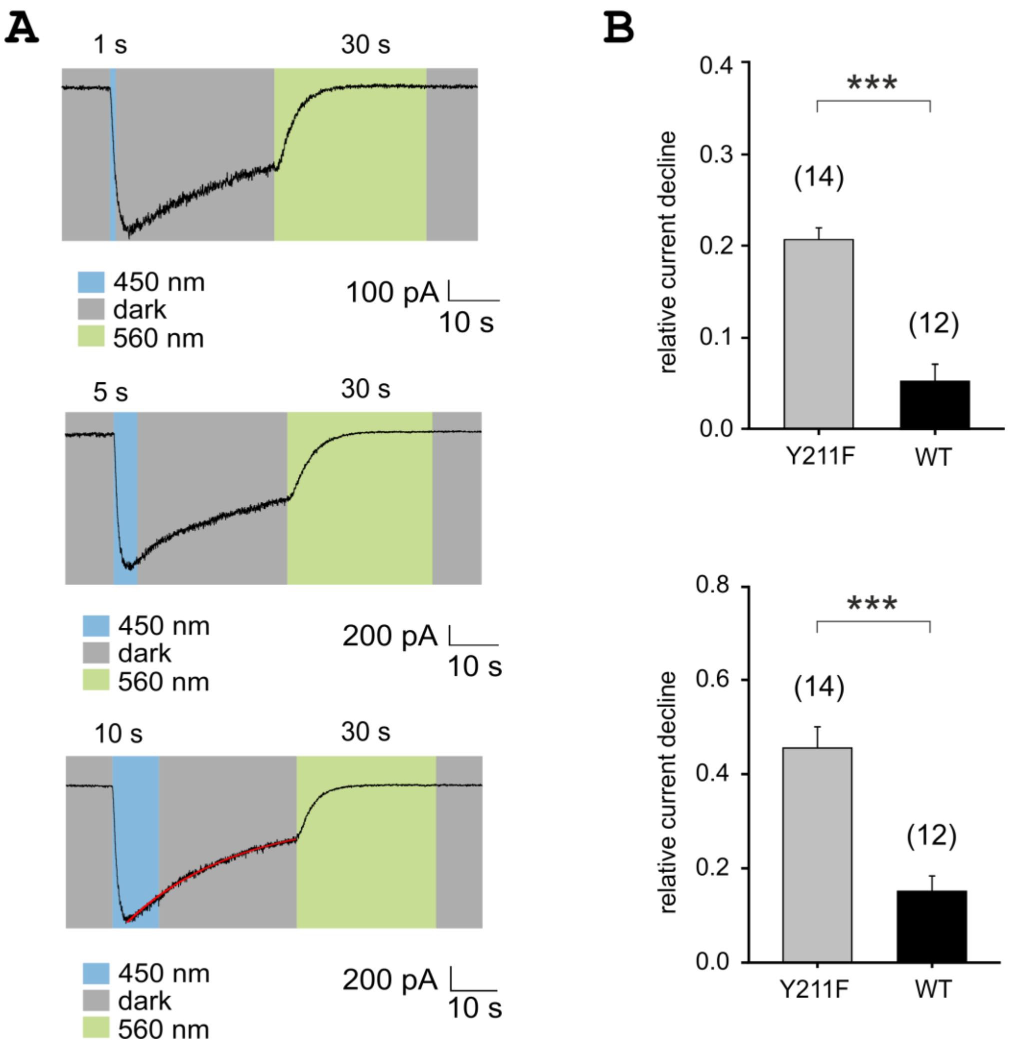

Figure S12: Decline of light induced GIRK currents. A light-induced GIRK current with 1 s (top), 5 s (middle) and 10 s (bottom) of 450 nm (1.6 mW/mm^2) light activation and 30 s 560 nm deactivation **B** Comparison of relative current decline of Y211F and mouse melanopsin, 10 s after activation (top) and 30 s after activation (bottom). The red line represents the exponential fit for current decline.

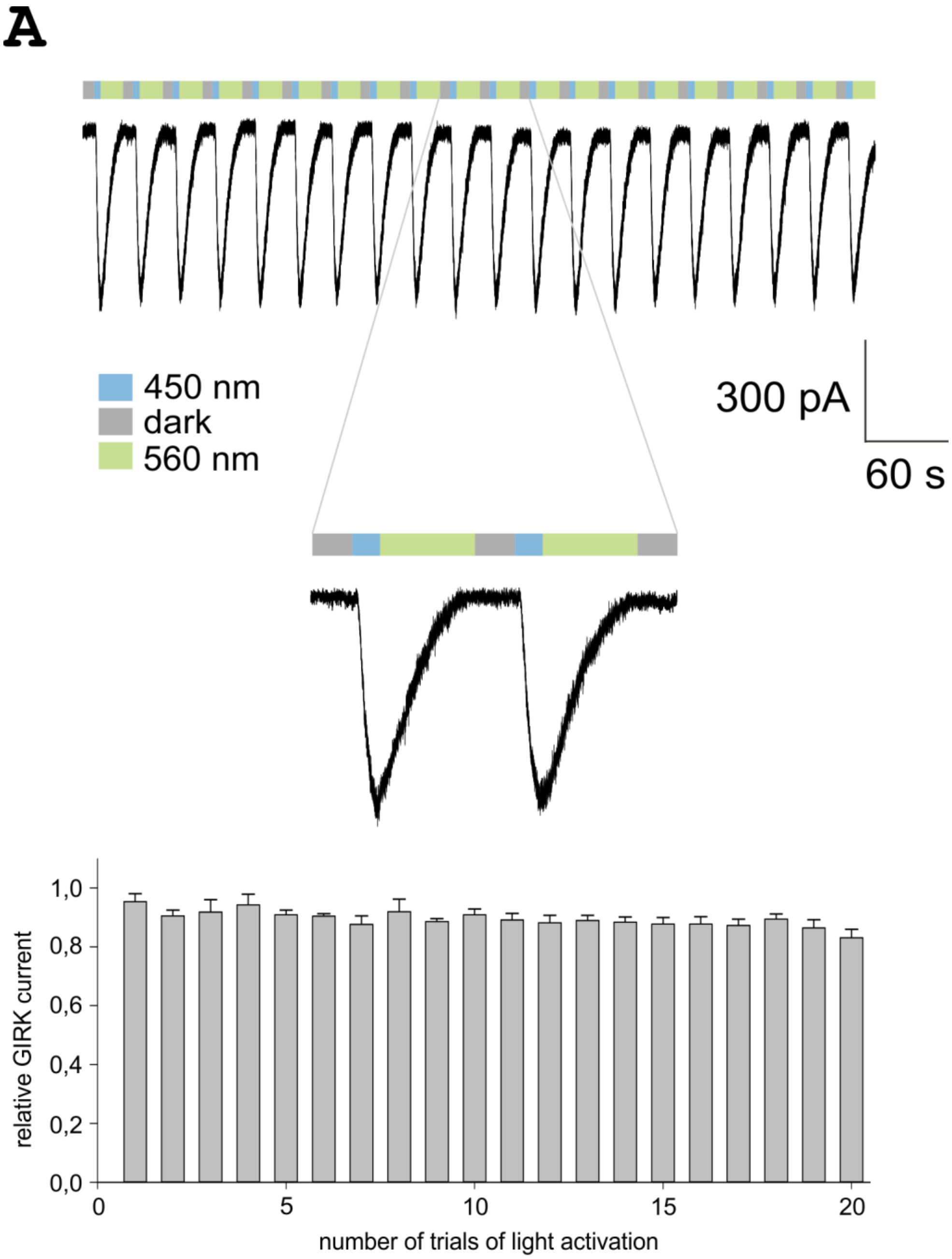

Figure S13: Repetitive light activation of Y211F. A patch clamp traces of repetitive activation and deactivation of the mutant. For the activation 10 s 450 nm (1.6 mW/mm^2) light pulse was used and for the deactivation 30 s of 560 nm. **B** maximal light induced GIRK current during repetitive light activation.

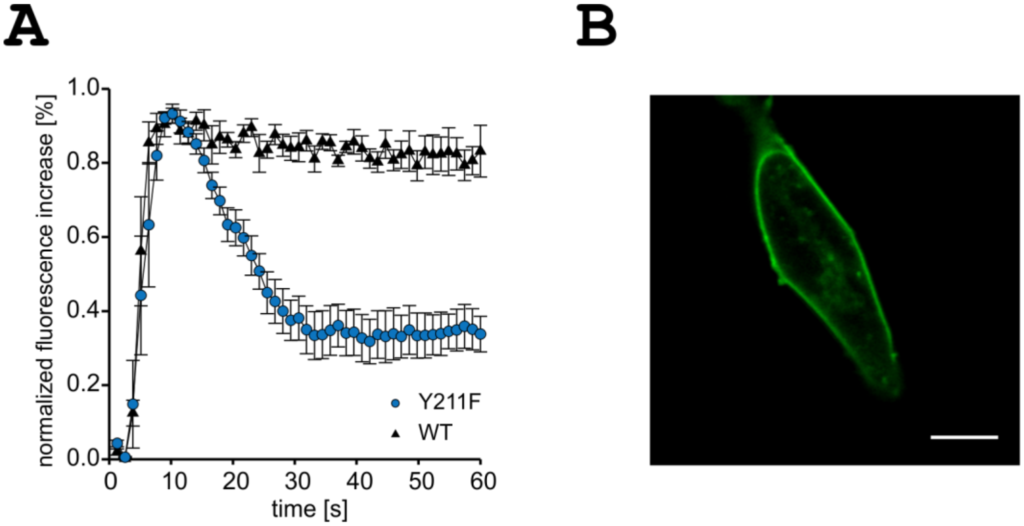

Figure S14: Y211F induced intracellular Ca^{2+} response in HEK cells. A Light-Induced Changes in Intracellular Ca^{2+} Levels with GCaMP6 in HEK TSA cells **B** 24 h expression of Opn4L-Y211F-eGFP in HEK cells, scale bar 5 µm.

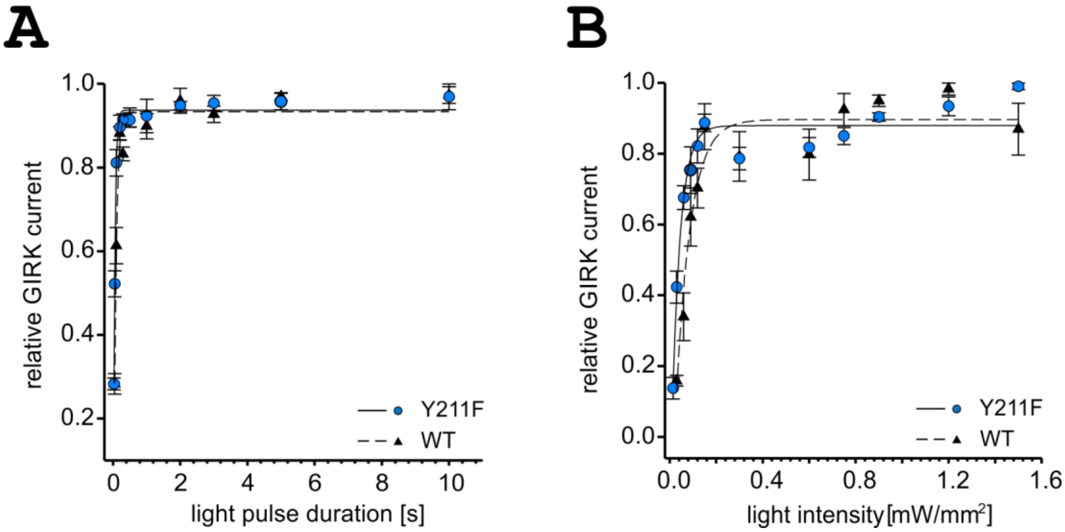

Figure S15: Light pulse duration and light intensity dependency of Y211F induced GIRK current in HEK293 cells. A Light pulse duration for light-induced GIRK currents using light pulses in a range of 30 ms to 10 s. For the deactivation a 30 s of 560 nm light pulse was applied. **B** Intensity dependency of GIRK current activation. Activation was elicited by 10 s light pulses of different intensities. For the deactivation 30 s 560 nm light pulse of maximal intensity was used.

References

[1] I. Radu, C. Bamann, M. Nack, G. Nagel, E. Bamberg, J. Heberle, *J. Am. Chem. Soc.* **2009**, *131*, 7313–7319.

[2] K. Spoida, D. Eickelbeck, R. Karapinar, T. Eckhardt, M. D. Mark, D. Jancke, B. V. Ehinger, P. König, D. Dalkara, S. Herlitze, et al., *Current Biology* **2016**, *26*, 1206–1212.

[3] J. C. Grieger, V. W. Choi, R. J. Samulski, *Nat Protoc* **2006**, *1*, 1412–1428.

[4] O. Volkov, K. Kovalev, V. Polovinkin, V. Borshchevskiy, C. Bamann, R. Astashkin, E. Marin, A. Popov, T. Balandin, D. Willbold, et al., *Science* **2017**, *358*, eaan8862.

[5] M. Murakami, T. Kouyama, *Nature* **2008**, *453*, 363–367.

[6] U. Höweler, *MAXIMOBY*, CHEOPS, Altenberge, Germany, **2007**.

[7] K. Eisenhauer, J. Kuhne, E. Ritter, A. Berndt, S. Wolf, E. Freier, F. Bartl, P. Hegemann, K. Gerwert, *J. Biol. Chem.* **2012**, *287*, 6904–6911.

[8] J. Kuhne, K. Eisenhauer, E. Ritter, P. Hegemann, K. Gerwert, F. Bartl, *Angew. Chem. Int. Ed.* **2015**, *54*, 4953–4957.

[9] J. Kuhne, *Submitted* **2018**.

[10] D. A. Case, V. Babin, J. Berryman, R. M. Betz, Q. Cai, D. S. Cerutti, C. Iii, T. E, T. A. Darden, R. E. Duke, et al., **2014**.

[11] M. J. Abraham, T. Murtola, R. Schulz, S. Páll, J. C. Smith, B. Hess, E. Lindahl, *SoftwareX* **2015**, *1–2*, 19–25.

[12] A. Vedani, D. W. Huhta, *Journal of the American Chemical Society* **1991**, *113*, 5860–5862.

[13] W. L. Jorgensen, J. Chandrasekhar, J. D. Madura, R. W. Impey, M. L. Klein, *The Journal of Chemical Physics* **1983**, *79*, 926–935.

[14] H. W. Horn, W. C. Swope, J. W. Pitera, J. D. Madura, T. J. Dick, G. L. Hura, T. Head-Gordon, *The Journal of Chemical Physics* **2004**, *120*, 9665–9678.

[15] T. H. Schmidt, C. Kandt, *J. Chem. Inf. Model.* **2012**, *52*, 2657–2669.

[16] S. Dapprich, I. Komáromi, K. S. Byun, K. Morokuma, M. J. Frisch, *Journal of Molecular Structure: THEOCHEM* **1999**, *461–462*, 1–21.

[17] T. Vreven, K. Morokuma, Ö. Farkas, H. B. Schlegel, M. J. Frisch, *Journal of Computational Chemistry* **2003**, *24*, 760–769.

[18] T. Vreven, K. Morokuma, in *Annual Reports in Computational Chemistry* (Ed.: D.C. Spellmeyer), Elsevier, **2006**, pp. 35–51.

[19] M. J. Frisch, *Gaussian 09*, Gaussian, Inc., Wallingford CT, **2009**.

[20] D. Mann, U. Höweler, C. Kötting, K. Gerwert, *Biophysical Journal* **2017**, *112*, 66–77.

[21] K. Gerwert, D. Mann, C. Kötting, *Biological Chemistry* **2017**, *398*, 523–533.

[22] D. Mann, J. Güldenhaupt, J. Schartner, K. Gerwert, C. Kötting, *J. Biol. Chem.* **2018**, *293*, 3871–3879.

[23] W. Humphrey, A. Dalke, K. Schulten, *J Mol Graph* **1996**, *14*, 33–38, 27–28.

[24] J. V. Ribeiro, R. C. Bernardi, T. Rudack, J. E. Stone, J. C. Phillips, P. L. Freddolino, K. Schulten, *Scientific Reports* **2016**, *6*, 26536.

[25] J. C. Phillips, R. Braun, W. Wang, J. Gumbart, E. Tajkhorshid, E. Villa, C. Chipot, R. D. Skeel, L. Kalé, K. Schulten, *Journal of Computational Chemistry* **2005**, *26*, 1781–1802.

[26] J. Huang, A. D. MacKerell, *Journal of Computational Chemistry* **2013**, *34*, 2135–2145.

[27] A. Leaver-Fay, M. Tyka, S. M. Lewis, O. F. Lange, J. Thompson, R. Jacak, K. W. Kaufman, P. D. Renfrew, C. A. Smith, W. Sheffler, et al., in *Methods in Enzymology* (Eds.: M.L. Johnson, L. Brand), Academic Press, **2011**, pp. 545–574.

[28] K. W. Kaufmann, G. H. Lemmon, S. L. DeLuca, J. H. Sheehan, J. Meiler, *Biochemistry* **2010**, *49*, 2987–2998.

[29] S. Lindert, J. A. McCammon, *J. Chem. Theory Comput.* **2015**, *11*, 1337–1346.

[30] A. Šali, T. L. Blundell, *Journal of Molecular Biology* **1993**, *234*, 779–815.

[31] J. B. Foresman, M. Head-Gordon, J. A. Pople, M. J. Frisch, *The Journal of Physical Chemistry* **1992**, *96*, 135–149.

[32] R. Bauernschmitt, R. Ahlrichs, *Chemical Physics Letters* **1996**, *256*, 454–464.

[33] M. E. Casida, C. Jamorski, K. C. Casida, D. R. Salahub, *The Journal of Chemical Physics* **1998**, *108*, 4439–4449.

[34] R. E. Stratmann, G. E. Scuseria, M. J. Frisch, *The Journal of Chemical Physics* **1998**, *109*, 8218–8224.

[35] C. Van Caillie, R. D. Amos, *Chemical Physics Letters* **1999**, *308*, 249–255.

[36] C. Van Caillie, R. D. Amos, *Chemical Physics Letters* **2000**, *317*, 159–164.

[37] F. Furche, R. Ahlrichs, *The Journal of Chemical Physics* **2002**, *117*, 7433–7447.

[38] G. Scalmani, M. J. Frisch, B. Mennucci, J. Tomasi, R. Cammi, V. Barone, *The Journal of Chemical Physics* **2006**, *124*, 094107.

[39] R. Ditchfield, W. J. Hehre, J. A. Pople, *The Journal of Chemical Physics* **1971**, *54*, 724–728.

[40] W. J. Hehre, R. Ditchfield, J. A. Pople, *The Journal of Chemical Physics* **1972**, *56*, 2257–2261.

[41] P. C. Hariharan, J. A. Pople, *Theoret. Chim. Acta* **1973**, *28*, 213–222.

[42] P. C. Hariharan, J. A. Pople, *Molecular Physics* **1974**, *27*, 209–214.

[43] M. S. Gordon, *Chemical Physics Letters* **1980**, *76*, 163–168.

[44] M. M. Francl, W. J. Pietro, W. J. Hehre, J. S. Binkley, M. S. Gordon, D. J. DeFrees, J. A. Pople, *The Journal of Chemical Physics* **1982**, *77*, 3654–3665.

[45] R. C. Binning, L. A. Curtiss, *Journal of Computational Chemistry* **1990**, *11*, 1206–1216.

[46] J.-P. Blaudeau, M. P. McGrath, L. A. Curtiss, L. Radom, *The Journal of Chemical Physics* **1997**, *107*, 5016–5021.

[47] V. A. Rassolov, J. A. Pople, M. A. Ratner, T. L. Windus, *The Journal of Chemical Physics* **1998**, *109*, 1223–1229.

[48] V. A. Rassolov, M. A. Ratner, J. A. Pople, P. C. Redfern, L. A. Curtiss, *Journal of Computational Chemistry* **2001**, *22*, 976–984.

[49] W. Thiel, *J. Am. Chem. Soc.* **1981**, *103*, 1413–1420.

[50] M. Reinsch, U. Höweler, M. Klessinger, *Journal of Molecular Structure: THEOCHEM* **1988**, *167*, 301–306.

[51] P. K. Janert, *Gnuplot in Action: Understanding Data with Graphs*, Manning, **2010**.

[52] K. Oda, J. Vierock, S. Oishi, S. Rodriguez-Rozada, R. Taniguchi, K. Yamashita, J. S. Wiegert, T. Nishizawa, P. Hegemann, O. Nureki, *Nature Communications* **2018**, *9*, 3949.

[53] J. Y. Lin, P. M. Knutsen, A. Muller, D. Kleinfeld, R. Y. Tsien, *Nature Neuroscience* **2013**, *16*, 1499–1508.

[54] R. H. Lozier, R. A. Bogomolni, W. Stoeckenius, *Biophys J* **1975**, *15*, 955–962.

[55] B. C. Goh, J. A. Hadden, R. C. Bernardi, A. Singharoy, R. McGreevy, T. Rudack, C. K. Cassidy, K. Schulten, *Annual Review of Biophysics* **2016**, *45*, 253–278.

[56] A. Schweitzer, A. Aufderheide, T. Rudack, F. Beck, G. Pfeifer, J. M. Plitzko, E. Sakata, K. Schulten, F. Förster, W. Baumeister, *PNAS* **2016**, *113*, 7816–7821.

[57] M. Wehmer, T. Rudack, F. Beck, A. Aufderheide, G. Pfeifer, J. M. Plitzko, F. Förster, K. Schulten, W. Baumeister, E. Sakata, *PNAS* **2017**, 201621129.

[58] Q. Guo, C. Lehmer, A. Martínez-Sánchez, T. Rudack, F. Beck, H. Hartmann, M. Pérez-Berlanga, F. Frottin, M. S. Hipp, F. U. Hartl, et al., *Cell* **2018**, *172*, 696-705.e12.

[59] M. Stemmer, T. Thumberger, M. del S. Keyer, J. Wittbrodt, J. L. Mateo, *PLOS ONE* **2015**, *10*, e0124633.

[60] H. Zhang, A. Qiao, D. Yang, L. Yang, A. Dai, C. de Graaf, S. Reedtz-Runge, V. Dharmarajan, H. Zhang, G. W. Han, et al., *Nature* **2017**, *546*, 259–264.

[61] Y.-L. Liang, M. Khoshouei, M. Radjainia, Y. Zhang, A. Glukhova, J. Tarrasch, D. M. Thal, S. G. B. Furness, G. Christopoulos, T. Coudrat, et al., *Nature* **2017**, *546*, 118–123.

[62] S. G. F. Rasmussen, B. T. DeVree, Y. Zou, A. C. Kruse, K. Y. Chung, T. S. Kobilka, F. S. Thian, P. S. Chae, E. Pardon, D. Calinski, et al., *Nature* **2011**, *477*, 549–555.

[63] P. Scheerer, J. H. Park, P. W. Hildebrand, Y. J. Kim, N. Krauß, H.-W. Choe, K. P. Hofmann, O. P. Ernst, *Nature* **2008**, *455*, 497–502.

[64] J. V. Ribeiro, R. C. Bernardi, T. Rudack, K. Schulten, E. Tajkhorshid, *Biophysical Journal* **2018**, *114*, 673a–674a.

[65] L. G. Trabuco, E. Villa, K. Mitra, J. Frank, K. Schulten, *Structure* **2008**, *16*, 673–683.

[66] S. Sekharan, J. N. Wei, V. S. Batista, *J. Am. Chem. Soc.* **2012**, *134*, 19536–19539.

[67] A. Krogh, B. Larsson, G. von Heijne, E. L. L. Sonnhammer, *Journal of Molecular Biology* **2001**, *305*, 567–580.

[68] F. Sievers, A. Wilm, D. Dineen, T. J. Gibson, K. Karplus, W. Li, R. Lopez, H. McWilliam, M. Remmert, J. Söding, et al., *Molecular Systems Biology* **2011**, *7*, 539.

[69] O. A. Masseck, K. Spoida, D. Dalkara, T. Maejima, J. M. Rubelowski, L. Wallhorn, E. S. Deneris, S. Herlitze, *Neuron* **2014**, *81*, 1263–1273.

[70] D. Kojima, S. Mori, M. Torii, A. Wada, R. Morishita, Y. Fukada, *PLOS ONE* **2011**, *6*, e26388.

[71] N. C. Klapoetke, Y. Murata, S. S. Kim, S. R. Pulver, A. Birdsey-Benson, Y. K. Cho, T. K. Morimoto, A. S. Chuong, E. J. Carpenter, Z. Tian, et al., *Nat Meth* **2014**, *11*, 338–346.

[72] K. Spoida, O. A. Masseck, E. S. Deneris, S. Herlitze, *PNAS* **2014**, 201321576.